POLITECNICO DI TORINO

Corso di Laurea Magistrale in Communications and Computer Networks Engineering

Tesi di Laurea Magistrale

Study of Advanced Techniques for Simultaneous Transmission of PN Ranging and High Bit Rate

Relatori:
Prof. Roberto Garello,
Dott. Andrea Modenini,
Prof. Guido Montorsi

Candidato:
Barbara Ripani

Anno Accademico 2020/2021

Contents

List of Figures

List of Tables

Acknowledgments

This thesis is the result of a collaboration between Politecnico di Torino and the European Space Research and Technology Centre (ESTEC) of the European Space Agency. I would first like to thank my academic supervisors, Professor Roberto Garello, who gave me this incredible opportunity and was a reference all along my internship, and Professor Guido Montorsi for his collaboration. I am grateful for the chance I had to be involved in such an inspiring working environment and glad for the colleagues I met. I wish to extend my special thanks to Dr. Andrea Modenini for his technical support on this work and for the trust he placed in me. Last but not least, I would like to thank my family and friends for their encouragement and support all through my studies.

Introduction

In all the scientific missions, the payload constitutes the ultimate purpose of the space mission itself. It refers to those elements of the spacecraft (e.g., scientific instruments) that generate mission data (payload data). The Payload Data Transmission (PDT [6], also known as high-rate telemetry) is of paramount importance for the mission's goal, and it is in the order of Mbps. Not least is the Telemetry, Tracking, and Command (TT&C [6]) function, which requires data rates in the order of kbps, and ensures the proper functioning of the spacecraft through the transmission down to the Earth of its status, the location determination, and the reception of critical commands transmitted from Earth. Orbit determination function, included in TT&C, lies at the basis of spacecraft navigation, and is achieved through ranging techniques based on the transmission of ranging signals.

Pseudo-Noise (PN) Ranging [2] [7] is a state-of-the-art positioning technique, standardized by the Consultative Committee for Space Data Systems (CCSDS), and recently introduced in Space Research (SR) missions, first with Bepi Colombo, followed by Solar Orbiter. The standard envisions simultaneous transmission of PN Ranging with high-rate telemetry modulated using Gaussian Minimum Shift Keying (GMSK). In this way, the Ground Station can determine the spacecraft's position by tracking the ranging sequence while receiving high-rate telemetry stream.

It is standard that TT&C transmission takes place in the X-Band (8-8.5 GHz) [8] using residual carrier modulation schemes. Differently, PDT transmissions can be either in X-Band (8-8.5 GHz) or in K-Band (26-28 GHz) [8]. In the former, the spacecraft has an integrated X-Band telecommunication subsystem that performs both the TT&C and PDT function, denoted as "X/X". This option is quite attractive for having greater mass, power, and cost savings for the mission. However, the Space Frequency Coordination Group (SFCG) recommendation limits the occupied bandwidth for X-Band Space Research (SR) transmission to 10 MHz [9], limiting the maximum bit-rate to less than 10 Mbps. Alternatively, to support a higher data rate, the spacecraft can resort to the "X/K" option, i.e., embed an additional transmission system in K-Band for implementing the sole PDT function. Clearly, this comes at the price of higher procurement costs (millions of Euro) and higher spacecraft mass and power consumption. Hence, this solution is only viable for large space missions where cost is not the main concern. Instead, for the most common medium/small missions that are mass, cost, and power limited, the only solution is the X/X option, constraining the payload data generation and thus tailoring the mission's scientific objectives.

Within this context, this thesis aims at overcoming the data rate bound, proposing a new communication architecture able to combine high-order modulations (QPSK, 8PSK, 16APSK, 32APSK, and 64APSK, included in the so-called SCCC standard [10] [5]) with PN Ranging signals. Namely, a receiver scheme that can simultaneously demodulate the PSK/APSK stream while tracking the PN ranging sequence was defined. For this purpose, a closed-loop parallel cancellation of the PN Ranging over the telemetry symbols and vice-versa was performed. The ranging accuracy validated by the innovative scheme is comparable to the standard approach of using GMSK, proving that the proposed solution has the potential to replace the classical design providing data rates that rise above the current limit.

This thesis is organized as follows: Chapter 1 introduces basic concepts of ranging techniques, while the detailed explanation of the PN Ranging is given in Chapter 2. Chapter 3 recalls the fundamentals of the GMSK modulation and its combination with the PN Ranging as stated by the standard. Next, Chapter 4 presents the innovative communication architecture that foresees the coupling of high-order modulations and PN Ranging, along with the numerical results obtained by simulating the complete transmitter-receiver chain. Finally, Chapter 5 analyses the applicability of the proposed communication scheme for two actual space mission scenarios: GAIA and GAIA-NIR [11] [3].

Chapter 1

Basics of Ranging

At the basis of space navigation lies the knowledge of the spacecraft's position and velocity, either relative to a Ground Station (G/S), to another spacecraft (S/C), or its target. To estimate these quantities, ranging systems are fundamental. Usually, a "two-way" ranging approach is used: a ranging signal is transmitted from the G/S to the S/C and back to the Earth (see Fig. 1.1). Then, the distance measurement is performed by estimating the time the ranging signal takes to make a round trip time to the spacecraft. Instead, the spacecraft's radial velocity is measured through the signal's Doppler shift, i.e., the frequency shift due to relative movement between the G/S and the S/C.

Focusing on the distance measurement, at the Earth-station, the telecommand carrier is coupled with a ranging signal that adopts specific frequency tones. These last are coherently demodulated at the spacecraft and then re-coupled with the telemetry carrier before being transmitted to the G/S, where, the received ranging signal will be out of phase with the transmitted one. This phase difference can be exploited to estimate the round-trip time, and therefore, the range to the spacecraft. Depending on the ranging technique, different tones are employed by generating the fixed or variable frequency tones, or, modulating a PN sequence. For instance, in the first case, the tone is a purely sinusoidal wave of frequency f, and the distance from

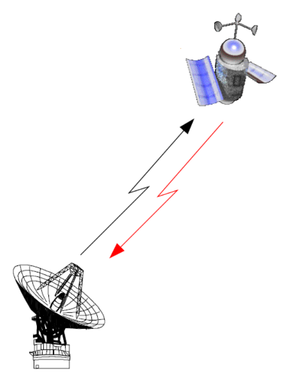

Figure 1.1: Two-way Ranging [1].

the satellite is derived from the phase shift between the transmitted and received tones [12]. Mathematically,

$$\Delta\phi = \frac{2\pi f}{c} \cdot 2R\,, \tag{1.1}$$

where, $2R$ is the round-trip range, c the speed of light and $\Delta\phi$ the phase shift. Because of the periodicity of the phase shift, there is an ambiguity in the range measurement that can be resolved by a proper choice of frequency. To increase measurement accuracy, one should resort to the use of high frequencies. On the other hand, ambiguity is no longer a concern only for those wavelengths that are much longer than the distance to be measured. Therefore, the further away the satellite is, the lower the frequency should be to reduce ambiguity in the range. Thus, there is a trade-off between choosing high and low frequencies: the former provide the best accuracy at the expense of increasing the ambiguity. Instead, the latter consent to resolve the ambiguity while decreasing the accuracy. Thus, to maximize the performance, multiple tones are simultaneously transmitted. Geostationary satellites, for example, have a major frequency tone around 100 kHz [12]. Even though a fixed frequency tone has been taken as an example, these concepts can be easily generalized to other ranging techniques.

Chapter 2

Pseudo-Noise Ranging

Pseudo-Noise (PN) Ranging is a particular type of ranging where the ranging sequence is a logical combination of the so-called range clock-sequence and several PN sequences. It is possible to distinguish two approaches to PN Ranging: transparent and regenerative ranging.

In the first, which is also the oldest, the spacecraft acquires the ranging signal and, without any further processing, re-modulates the entire passband including uplink noise onto the downlink carrier. Then, the receiver station acquires and demodulates the downlink signal, correlating the received ranging signal with a local replica to determine the round-trip light time. Since there is no uplink noise removal at the spacecraft transponder, the use of the transparent ranging may be limited to scenarios where there is a very good link margin or where the accuracy is not of primary concern. To be more precise, the signal-to-noise ratio (SNR) at the station is proportional to $1/r^4$, where r is the distance to be measured [2]. On the other hand, transparent ranging has the advantage that can be easily implemented in the transponder by means of simple filtering of the ranging signal (the so-called "transparent channel").

Instead, in regenerative ranging, after signal acquisition, the spacecraft demodulates and regenerates the ranging code coherently with the uplink one. Then, this local replica is modulated and sent back to the G/S. At this point, the receiving station operates identically to the transparent ranging, but will experience an SNR proportional to $1/r^2$ [2], hence providing a much higher measurement accuracy. However, this comes at the price of adding complexity to the spacecraft transponder.

This chapter focuses on the basics of PN Ranging, namely, its code structure, generation, modulation, and shaping, and its properties. Following this introduction, an overview of the code acquisition and tracking is presented.

2.1 Code Structure

PN Ranging code results from a logical combination of the ranging clock with several component PN sequences. In this respect, the CCSDS defined a PN Ranging standard [2] that foresees six binary PN sequences, each having period L_i, for $i = 1, ..., 6$, that have interesting correlation properties. In Tab. 2.1, the significant sequences are reported, along with their period. The range clock is a periodic binary sequence with a period of 2 chips that has the highest frequency and, thus, it determines the range measurement resolution. If on one hand, the higher its frequency,

Code	Period	Chips
C_1	2	+1 –1
C_2	7	+1 +1 +1 –1 –1 +1 –1
C_3	11	+1 +1 +1 –1 –1 –1 +1 –1 +1 +1 –1
C_4	15	+1 +1 +1 +1 –1 –1 –1 +1 –1 –1 +1 +1 –1 +1 –1
C_5	19	+1 +1 +1 +1 –1 +1 –1 +1 –1 –1 –1 –1 +1 +1 –1 +1 +1 –1 –1
C_6	23	+1 +1 +1 +1 +1 –1 +1 –1 +1 +1 –1 –1 +1 +1 –1 –1 +1 –1 +1 –1 –1 –1 –1

Table 2.1: Component PN sequences.

the more accurate the measurement is, on the other hand, high frequencies (shorter periods) lead to ambiguous ranges. To overcome this problem, the ranging clock is combined with longer-period component PN sequences forming a composite code, obtained by two possible logical combinations of the sequences (later explained) dictated by the Weighted-voting parameter v.

A balanced Tausworthe 4B (T4B) is obtained for a Weighted-voting $v = 4$, while a balanced Tausworthe 2B (T2B) for $v = 2$. If the former is characterized by a strong ranging clock component which provides excellent ranging accuracy, at the expense of slightly longer acquisition time, the latter has a weak clock component that results in a shorter acquisition time for the ranging measurement but increased jitter [7]. Both of them can be used when dealing with regenerative ranging, whereas the choice is limited to T2B for transparent ranging [2].

2.2 Code Generation

Fig. 2.1 shows the block diagram of the PN code generation. Its six PN periodic components are reported in Tab. 2.1, and they are the same for T4B and T2B. The generation stage requires one circular shift register per PN component, each of them of length equal to their corresponding component's period, and clocked to the chip rate. Then, at each clock time, the outputs of the shift registers are combined according to the rule

$$c_k = \mathrm{sign}(vC_{1,k} + C_{2,k} - C_{3,k} - C_{4,k} + C_{5,k} - C_{6,k})\,, \tag{2.1}$$

where v is the vote assigned to the ranging clock (2 for T2B and 4 for T4B), $C_{i,k}$ the output of the i-th register at time k, and finally $c_k \in \{\pm 1\}$ is k-th PN code chip.

2.3 Modulation and Pulse Shaping

Once the transponder generates the PN code sequence, it is linearly phase modulated in the downlink carrier. Therefore, the alternation of ± 1 of the ranging code translates into a phase shift of the RF carrier signal.

For preserving the bandwidth, a sinusoidal shaping filter $h(t)$ is applied to the baseband

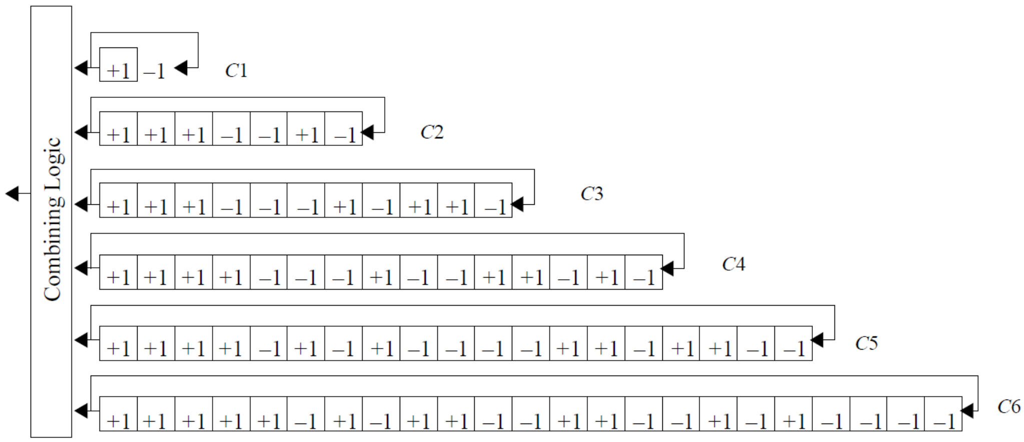

Figure 2.1: Regenerative PN code generation [2].

signal, illustrated in Fig. 2.2, and mathematically described by

$$h(t) = \begin{cases} \sin(\pi t/T_c) & t \in [0, T_c] \\ 0 & \text{elsewhere} \end{cases}, \tag{2.2}$$

where T_c is the chip time.
The phase of the modulated PN Ranging signal is

$$\Phi_{RG}(t) = m_{RG} \sum_k c_k h(t - kT_c)\,, \tag{2.3}$$

being m_{RG} the modulation index [2].

2.4 Code Properties

This section provides an overview of PN Ranging code properties, with regards to its length, imbalance, correlation, and spectra.

Code Length

The composite code length is

$$\begin{aligned} L &= \prod_i L_i & (2.4) \\ &= 2 \cdot 7 \cdot 11 \cdot 15 \cdot 19 \cdot 23 = 1\,009\,470 \text{ [chips]}\,, & (2.5) \end{aligned}$$

which is nothing else than the product of the length L_i of each composite PN sequence. It can be noticed that is the same for both the T4B and the T2B.

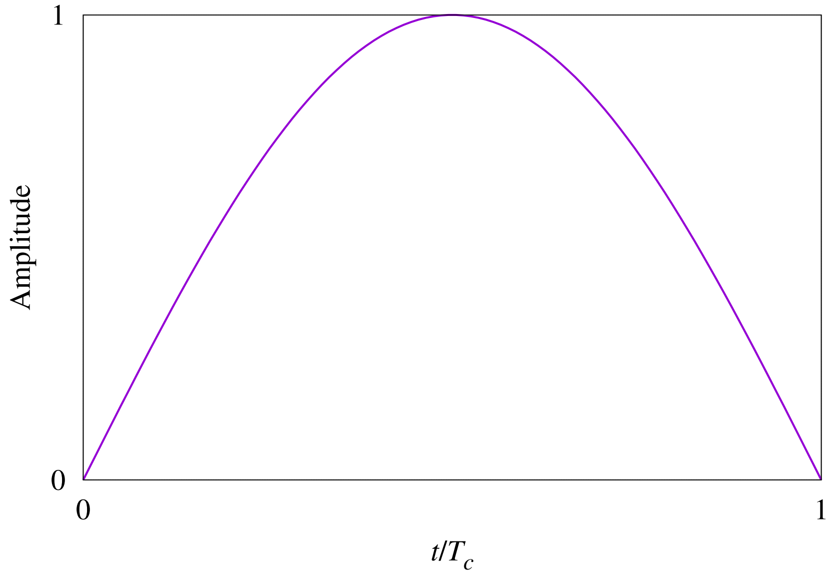

Figure 2.2: Sinusoidal pulse shape filter.

Generation scheme	Number of +1s	Number of −1s	Imbalance
T4B	504583	504887	304
T2B	504033	505437	1404

Table 2.2: Code imbalance for T4B and T2B schemes computed for $L = 1009470$.

Code Imbalance

It can be shown (see Tab. 2.2) that the number of +1s does not match the number of −1s in the composite code and therefore, it is unbalanced. Thus, despite the choice of scheme, the PN code spectrum presents an undesired DC component that, if not filtered out, can lead to distortions, and thus, errors. Moreover, the energy in the DC component cannot be used for ranging. To mitigate these problems, the C_3, C_4, and C_6 components are inverted as in (2.1), reducing the code imbalance.

Correlation Properties

To investigate the correlation properties of a sequence, the in-phase and out-of-phase correlations are examined [7]. The former results from the perfect phase-alignment between the composite code and its component PN sequences. Instead, the latter is due to their phase misalignment, which ranges from 1 to $(L_i - 1)$ chips. The correlation values have been computed for each of the component PN sequences as follows. Each component PN code period has been repeated up to the composite code's length. Once obtained two sequences having the same length, the

Code	In-Phase Correlation		Out-Of-Phase Correlation	
	T4B	T2B	T4B	T2B
C_1	947566	633306	-947566	-633306
C_2	61904	247020	-10368	-41404
C_3	61904	250404	-6160	-24900
C_4	61904	251332	-4400	-17852
C_5	61904	251604	-3456	-14056
C_6	61904	251940	-2800	-11388

Table 2.3: In-Phase and Out-Of-Phase correlation for T4B and T2B.

component PN sequence has been multiplied chip by chip with the ranging code, and the result summed up (in-phase correlation). The procedure has been then repeated $L_i - 1$ times, this once by using a different cycle shift (from 1 up to $L_i - 1$ chips) of the component PN code. These last represent the out-of-phase correlation.

The results are shown in Tab. 2.3, where it can be seen a sharp discrepancy between the in-phase and the out-of-phase correlation values, essential for the receiving station to minimize the error when aligning the local replica to the received sequence and thus, in the computation of the delay (in chips) between the two.

Power Spectral Density

The Power Spectral Density (PSD) for the phase-modulated PN composite code, generated according to the T4B and T2B schemes, has been measured for the sinusoidal pulse shape using a modulation index of 0.75 rad-pk. The resulting plots for T4B and T2B, as function of the frequency normalized to the chip rate R_{RG}, are shown in Fig. 2.3 and 2.4 respectively.

The two spectra share the discrete component located at the zero frequency, which is due to the residual carrier. Additionally, the ranging clock component, located at one-half of the chip rate, is stronger in the T4B spectrum than in the T2B because of the larger vote v and therefore, higher power, provided to it. The most relevant criteria to choose one scheme over the other lies in the trade-off between acquisition time and measurement accuracy. In fact, the larger the vote allocated to the clock, the lower the power assigned to the longer PN sequences, resulting in a larger acquisition time and more precise range measure. Consequently, the T2B scheme should be employed when the acquisition time is of primary concern, whereas the T4B scheme is the most appropriate solution when the range accuracy is of primary concern [7].

2.5 Acquisition and Tracking of Ranging Codes

The acquisition of the ranging signal is done by means of a carrier tracking loop, whose output is used to lock on to the PN code through a bank of six correlators [7]. Each of them correlates the received ranging code with all the possible shifts of the related PN component. Within the L_i correlations, the maximum is searched to determine the phase shift of the received sequence. Only once all the six phases have been recovered, the phase of the acquired sequence is extracted and used, along with the estimated chip rate, to generate the local PN replica.

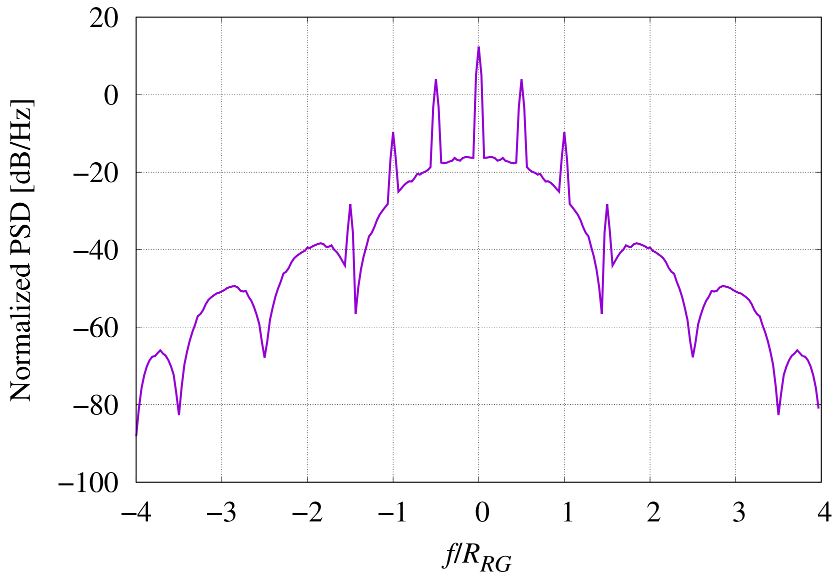

Figure 2.3: Power spectral density for T4B code scheme.

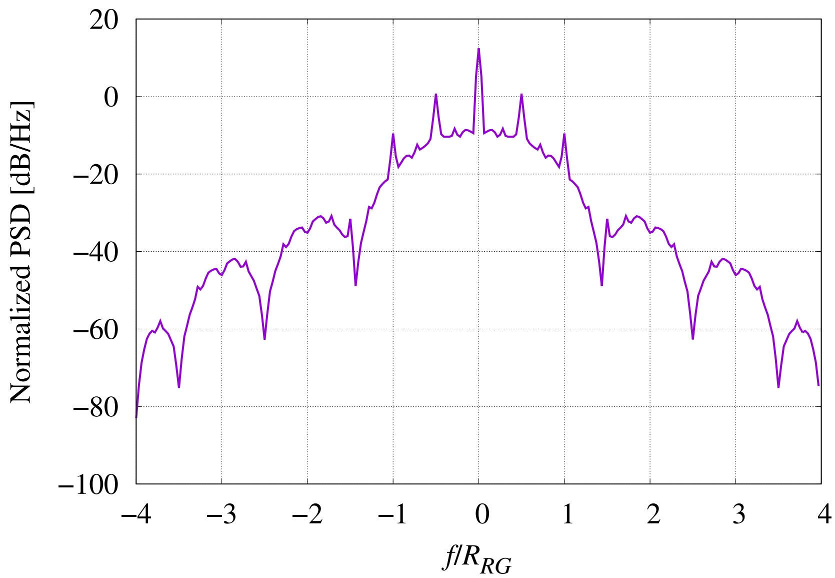

Figure 2.4: Power spectral density for T2B code scheme.

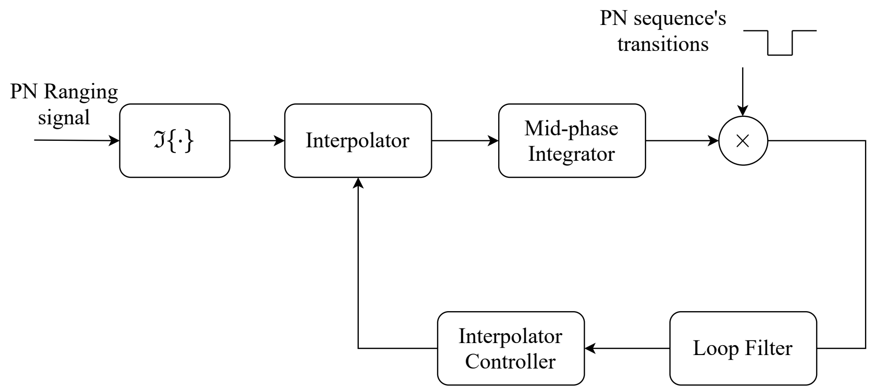

Figure 2.5: Chip tracking loop.

After the acquisition stage, the system must remain locked during all the reception time by tracking the chips. To achieve this, a Chip Tracking Loop (CTL) is used for timing estimation. Because of its nature, except for some 'transgressions' due to the small majority of -1 rather than $+1$, the composite PN code echoes a square wave. As a consequence, the CTL can be obtained by slightly modifying the Data Transition Tracking Loop (DTTL) [13]. According to the scheme in Fig. 2.5, the imaginary component of the received ranging signal first passes through a linear interpolator, the coefficients of which are re-computed based on the estimated timing error. Then, the interpolated chips go into the mid-phase integrator which computes the integral between pairs of adjacent chips. This operation is depicted in Fig. 2.6, where the mid-phase integrator (in red) is misaligned due to a timing error of ε_k with respect to the chip (shown as black solid lines). Thus, the output of the mid-phase integrator will be equal to $\pm 2\varepsilon_k\sqrt{P}$, where P is the useful power of the ranging signal.

The output of the mid-phase integrator is multiplied by the chip transition sequence in which a $+1$ indicates a positive chip followed by a negative one, a -1 a negative chip followed by a positive one, and a 0 that two consecutive chips have the same polarity. This operation allows to use the error ε_k to adjust the sampling time; for example, consider the reception of $+1$ followed by the reception of -1. If the output of the mid-phase integrator is positive, it means that the estimated sampling time is early with respect to the received code. Therefore, the sign of the error must be positive so that it can lead to a shift 'forward' of the sampling time. Instead, if the mid-phase integrator's output is negative, then the estimated sampling time is running late with respect to the received code, and a negative sign in the error would shift 'backward' the sampling time. Then, the resulting error is filtered through the Loop Filter, whose output is used to modify the operating point of a linear interpolator to correct the timing error.

For the sake of clarity, in the remainder of this thesis, the chip tracking loop has been implemented as a first-order loop. As such, its open-loop transfer function reads

$$H(z) = \frac{K}{1 - z^{-1}} \,, \tag{2.6}$$

and it has no zeroes and one pole only [14]. Considering the linearized model of the CTL presented in [7], shown in Fig. 2.7, the loop computes the k-th estimated sampling time $\hat{\tau}_k$ as the sum of the previous estimation $\hat{\tau}_{k-1}$ and the detected error ε_k weighted by the open-loop

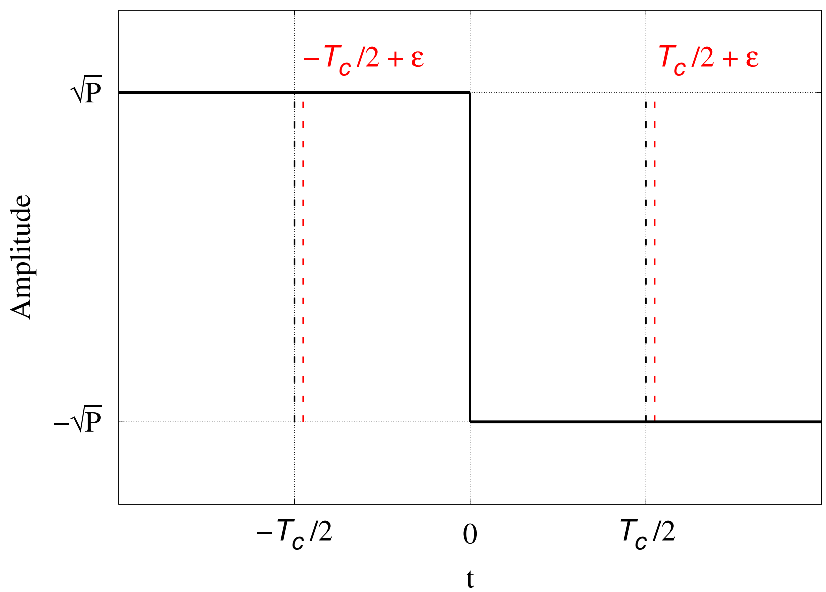

Figure 2.6: Mid-phase integration.

gain K, i.e.,

$$\hat{\tau}_k = \hat{\tau}_{k-1} + K\varepsilon_k \,. \tag{2.7}$$

The open-loop gain is defined as

$$K = K_\varepsilon \cdot \gamma \,, \tag{2.8}$$

where, $K_\varepsilon = 2\sqrt{P}$ represents the mid-phase integrator gain and γ the Loop Filter gain.

The parameter K is strictly related to the digital loop bandwidth defined as

$$2B_L T_s \triangleq \frac{1}{2\pi j} \oint_{|z|=1} \left(\frac{H(z)}{1+H(z)} \right) \cdot \left(\frac{H(1/z)}{1+H(1/z)} \right) \frac{\mathrm{d}z}{z} \,, \tag{2.9}$$

with T_s being the sampling interval. In [14] the integral in Eq. (2.9) has been evaluated for a Type 1, Order 1 Phase Locked Loop (PLL) and corresponds to

$$B_L = \frac{K}{4T_s} = \frac{\gamma\sqrt{P}}{2T_s} \,. \tag{2.10}$$

CTL performance depends on the chip pulse shape; it can be shown that the theoretical timing ranging variance used to evaluate the CTL performance is (see [7])

$$\sigma_\tau^2 = \begin{cases} \frac{1}{4} \cdot \frac{B_L {T_c}^2}{P/N_0 \,,} & \text{for a square pulse shape} \\ \\ \frac{1}{8} \cdot \frac{B_L {T_c}^2}{P/N_0 \,,} & \text{for a sine pulse shape} \end{cases} \,, \tag{2.11}$$

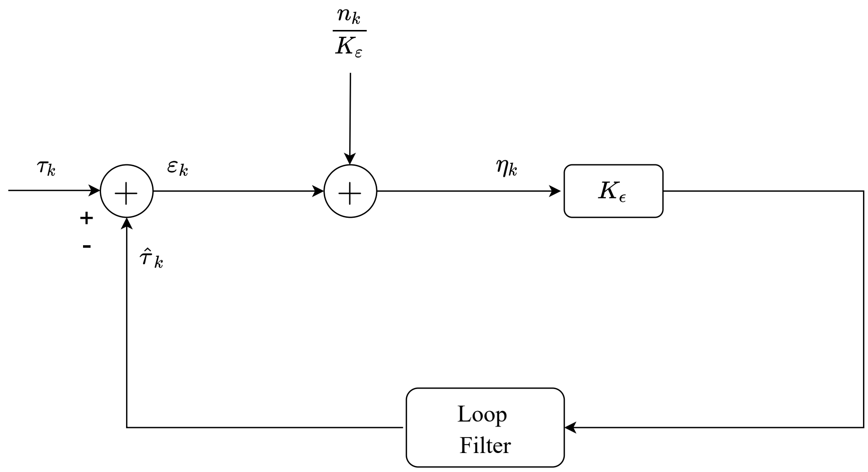

Figure 2.7: Linearized CTL model.

where P/N_0 is the ratio between the ranging power and the noise power spectral density. Normalizing σ_τ^2 with respect to T_c^2, the normalized ranging jitter $\widetilde{\sigma}_\tau^2$ is obtained. As can be deduced from Eq. s(2.11), CTL performance suffers when a square rather than sinusoidal pulse shape is used. For this reason, CCSDS recommends adopting only the sinusoidal pulse shape [2].

To exemplify this point, Fig. 2.8 shows the normalized ranging jitter $\widetilde{\sigma}_\tau^2$ of a CTL tuned by setting $\gamma = 10^{-2}$. Its timing jitter was computed by numerical simulations, and compared with the theoretical curves obtained from Eq. (2.11). It can be seen that a perfect matching between them was achieved.

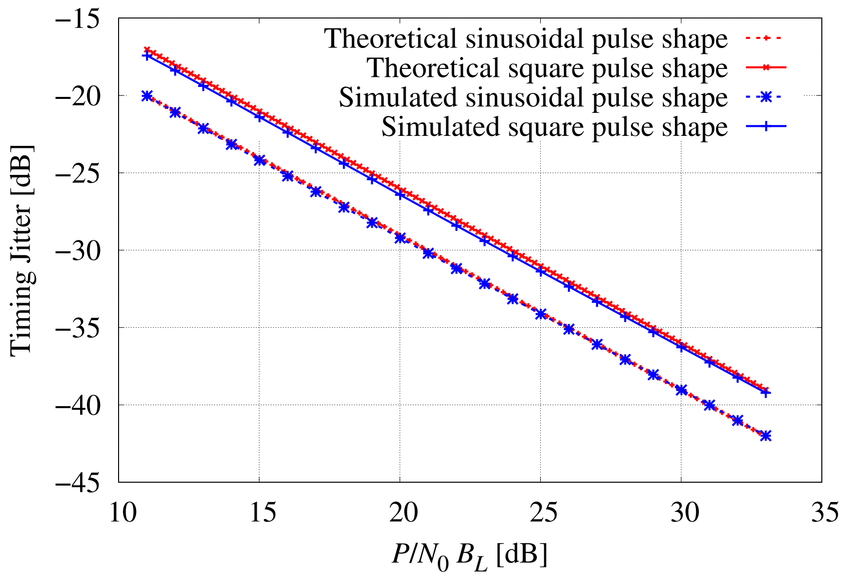

Figure 2.8: Effects of pulse shape on timing ranging jitter $\widetilde{\sigma}_\tau^2$.

Chapter 3

PN Ranging and GMSK

For data rates higher than 2 Msymbol/s in the 8400–8500 MHz Space Research Service (SRS) bands, CCSDS recommends [15] telemetry and ranging transmission to be performed simultaneously by using a Gaussian Minimum Shift Keying (GMSK, [16]) modulation scheme coupled with PN Ranging. In this case, the PN Ranging signal causes supplementary random phase shifts, and corrupts the recovery of the telemetry data acting as noise. Similarly, the erroneous demodulation of the telemetry symbols negatively impacts the detection of the ranging chips [17].

This chapter reviews this state-of-the-art technique that will serve as a benchmark for the rest of this thesis. First, an overview of GMSK modulation is presented. Then, the details of simultaneous transmission of PN Ranging and GMSK telemetry, along with their performance coming from numerical simulations, are provided.

3.1 GMSK Modulation

GMSK modulation is a modified version of Minimum Shift Keying (MSK) where, the unmodulated symbols are passed through a low pass filter (LPF) with a Gaussian shaping pulse instead of a rectangular window. This modification leads to a more compact power spectrum, with reduced side lobes, rather than in MSK, at the expense of introducing additional Inter-Symbol Interference (ISI).

GMSK is a Continuous Phase Modulation (CPM) with partial response (correlation length $L > 1$) and, as such, depending on the shaping pulse adopted, it may achieve a higher spectral efficiency than BPSK/QPSK modulation schemes. Nevertheless, what makes GMSK modulation attractive is its constant envelope characteristic, for limiting non-linear distortions due to power amplification [18].

GMSK modulation is characterized by a shaping pulse $g(t)$ obtained as a rectangular pulse filtered by a Gaussian filter. Such pulse shape reads

$$g(t) = \frac{1}{2T}\left[\mathrm{Q}\left(\frac{\pi B(t-\frac{T}{2})}{\sqrt{\ln 2}}\right) - \mathrm{Q}\left(\frac{\pi B(t+\frac{T}{2})}{\sqrt{\ln 2}}\right)\right], \tag{3.1}$$

where T is the symbol time, and B is the 3-dB Gaussian filter bandwidth.

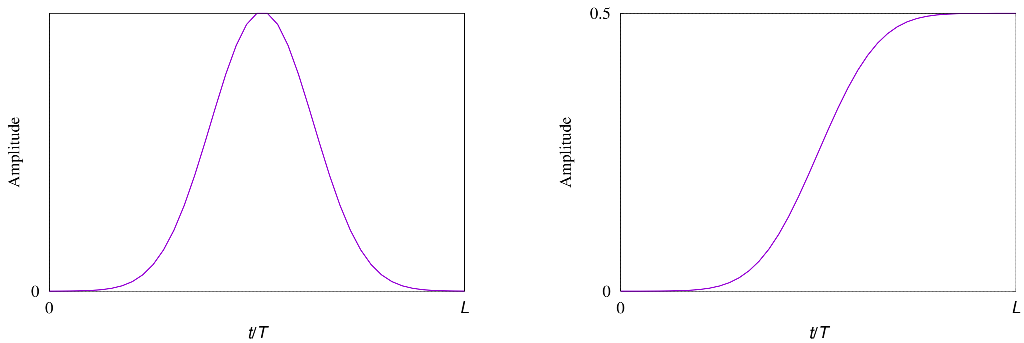

(a) Frequency pulse $g(t)$

(b) Phase pulse $q(t)$

Figure 3.1: GMSK frequency and phase pulses for $BT = 0.25$.

The product of the two defines the classical GMSK design parameter BT, i.e., the normalized filter bandwidth. The design parameter BT can take values in the range [0,1] and determines the width of the spectrum main lobe. The smaller BT is, the lesser the spectral occupancy will be. However, this comes at the cost of higher ISI and larger performance discrepancy between GMSK and MSK. The function $g(t)$ is referred to as the "frequency shape pulse", and by integration, it is possible to obtain the phase function

$$q(t) = \int_{-\infty}^{t} g(\tau)\mathrm{d}\tau \,, \tag{3.2}$$

which, along with the modulation index h and the information symbols, determines the phase variation along time. Even though the frequency pulse is defined in the interval $[-\infty, \infty]$, its energy is mainly concentrated in the interval $[-T, T]$ for $BT = 0.25$ [18]. Consequently, the phase function continuously changes in the same interval and reaches its maximum at time T. Fig. 3.1a and 3.1b illustrate $g(t)$ and $q(t)$ for $BT = 0.25$.

The information symbols $a_k \in \{\pm 1\}$ are embodied in the excess phase

$$\Phi_{TM}(t, \mathbf{a}) = 2\pi h \sum_{k=-\infty}^{\infty} a_k q(t - kT) + \theta \,, \tag{3.3}$$

which results in a weighted sum of shifted versions of $q(t)$. The modulation index h is equal to 0.5 for both MSK and GMSK modulation schemes. Because of its dependence on $q(t)$, $\Phi_{TM}(t, \mathbf{a})$ is a continuous time-varying function that introduces memory in the CPM signal. The first RHS term in (3.3) is called the instant phase, which is responsible for the total excess phase variation, whereas the second RHS term is the initial phase, a constant contribution. Recalling the general expression of the CPM signal,

$$s(t, \mathbf{a}) = \sqrt{\frac{2E_s}{T}} \exp\left(j\Phi_{TM}(t, \mathbf{a})\right) \tag{3.4}$$

where E_s is the symbol energy, then the resulting signal $s(t, \mathbf{a})$, besides the current one, will depend on the $L - 1$ previously transmitted symbols.

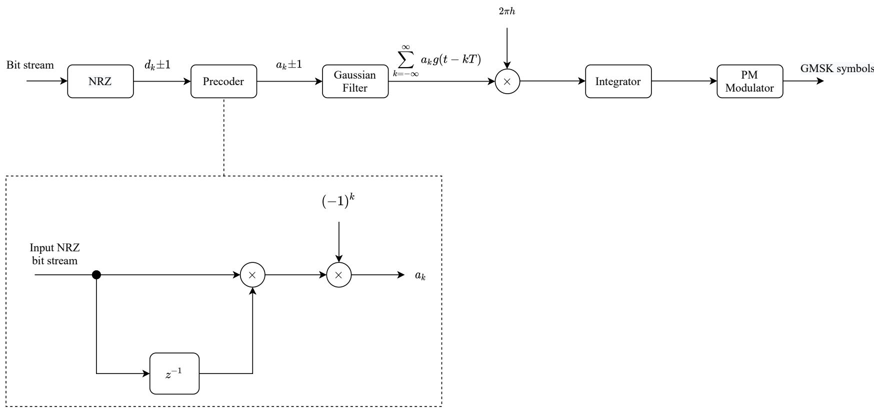

Figure 3.2: Block diagram of GMSK modulator.

3.1.1 Modulator

The GMSK modulator has been implemented according to the block diagram reported in Fig. 3.2. For generating the GMSK constellation, the input bitstream is mapped to Non-Return-to-Zero (NRZ) symbols $d_k \in \{\pm 1\}$, further processed by the precoder to obtain the precoded symbols a_k [19] as

$$a_k = (-1)^k \cdot d_k \cdot d_{k-1} \ , \tag{3.5}$$

where $d_{-1} = 1$.
The precoder output symbols are passed through a low pass filter with impulse response $g(t)$ and integrated to obtain the instant phase. Finally, the In-phase and Quadrature components are output to the PM modulator producing the GMSK symbols.

The Bit Error Rate (BER) curves (provided in Section 3.2) have been simulated and compared to the theoretical one, proving the correctness of the results. The scattering diagram after the modulator, in Fig. 3.3, shows the constant amplitude of the constellation points. Additionally, because the constellation points derive from a continuous-time succession, the figure also demonstrates the continuity of the phase variation. To stress the relationship between the BT parameter and the spectral occupancy, Fig. 3.4 shows the power spectral density for the GMSK modulation with $BT = 0.5$ and $L = 3$ (violet), and with $BT = 0.25$ and $L = 5$ (green). Since the lower the BT parameter, the longer the tails of the Gaussian impulse response will be, the ISI has a greater impact on $BT = 0.25$ rather than on $BT = 0.5$. Consequently, by properly choosing BT, it is possible to trade-off spectral occupancy for ISI reduction. Comparing the power spectra of Fig. 3.4 and 3.5, the impact of the Gaussian shaping pulse on the side lobes is unequivocal: there is a clear improvement in spectral efficiency of GMSK with respect to MSK.

3.1.2 Laurent Decomposition

As Pierre A. Laurent demonstrated, it is always possible to represent any constant envelope binary phase modulation as a linear combination of a finite sequence of amplitude modulated pulses (AMP) through the Laurent decomposition [20]. It is based on the generalized phase

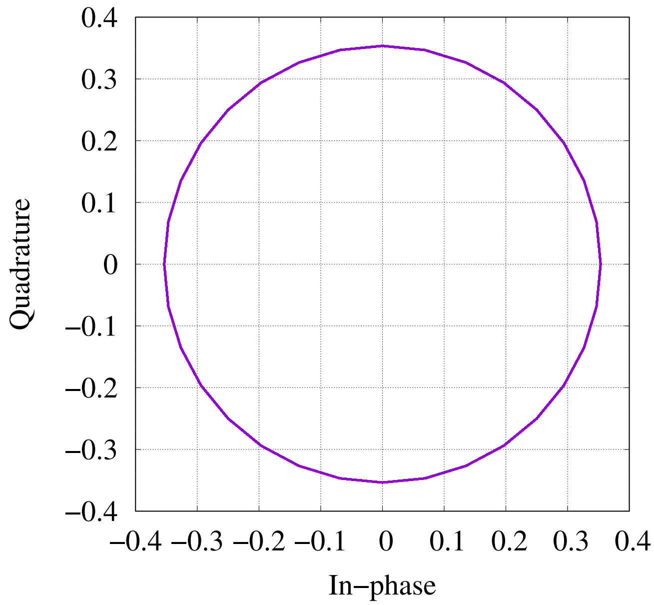

Figure 3.3: Scattering diagram for GMSK modulation.

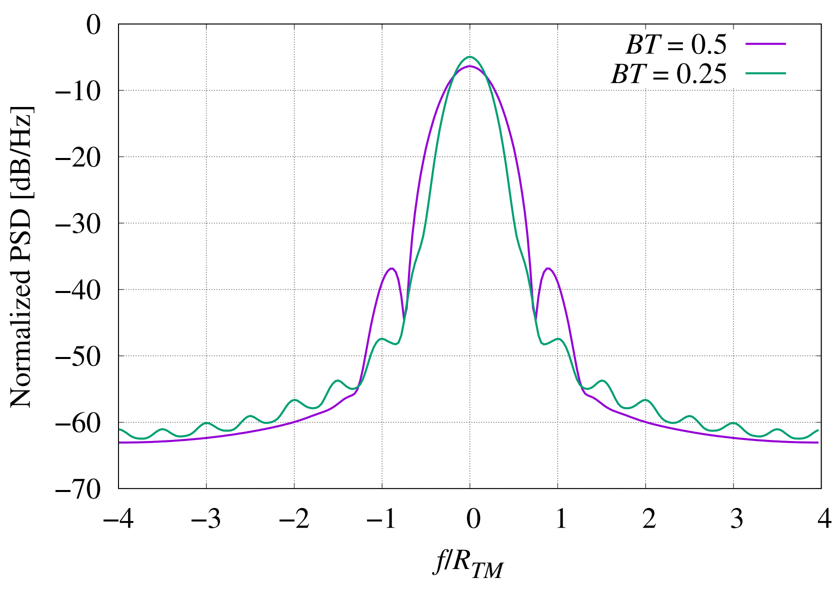

Figure 3.4: Power spectral density of GMSK.

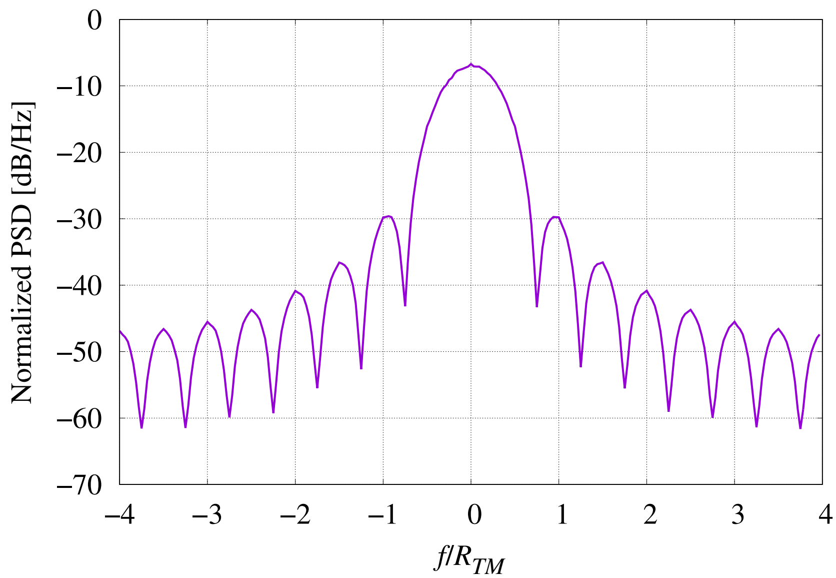

Figure 3.5: Power spectral density of MSK.

pulse function, described as

$$S_0(t) = \frac{\sin(\psi(t))}{\sin(\pi h)}\,, \tag{3.6}$$

where,

$$\psi(t) = \begin{cases} \sin(2\pi h q(t)) & t \in [0, LT] \\ \sin(\pi h - 2\pi h q(t - LT)) & t \in [LT, 2LT] \end{cases}\,. \tag{3.7}$$

Defining the function $S_n(t)$ as

$$S_n(t) \triangleq S_0(t + nT) = \frac{\sin(\psi(t + nT))}{\sin(\pi h)}\,, \tag{3.8}$$

the pulse sequence that approximate the CPM signal is obtained by means of the generalized shaping pulse function as

$$c_k(t) = S_0(t) \prod_{i=0}^{L-1} S_{i+L\beta_{k,i}(t)}\,, \tag{3.9}$$

where $\beta_{k,i}(t) \in \{0, 1\}$ and represent the $c_k(t)$ index

$$k = \sum_{i=1}^{L-1} 2^{i-1} \cdot \beta_{k,i}\,. \tag{3.10}$$

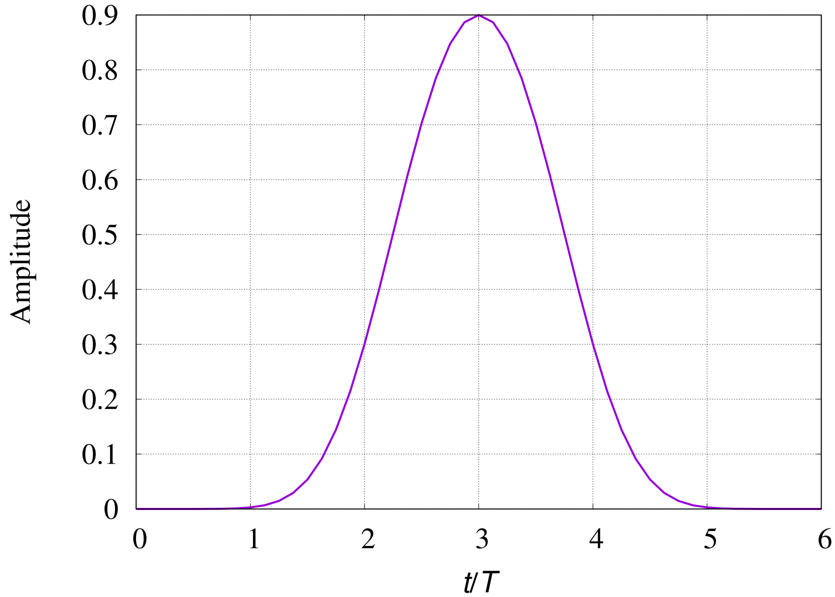

Figure 3.6: C_0 Laurent pulse for GMSK ($BT = 0.25$).

Finally, the complex envelope of the CPM signal in (3.4) can be seen as the sum of $Q = 2^{L-1}$ signals as [21]

$$s(t, \mathbf{a}) = \sum_{k=0}^{Q-1} \sum_{n} b_{k,n} c_k(t - nT)\,, \tag{3.11}$$

where $b_{k,n}$ are the so-called pseudo symbols, which are related to the information a_m symbols by

$$b_{k,n} = \exp\left[jh\pi \left(\sum_{m=-\infty}^{n} a_m - \sum_{i=0}^{L-1} a_{n-i}\beta_{k,i} \right) \right]. \tag{3.12}$$

Since $c_0(t)$ contains most of the signal energy [20], it can be concluded that any GMSK signal can be approximated by a linear modulation having expression

$$s(t, \mathbf{a}) \sim \sum_{n} b_{0,n} c_0(t - nT)\,. \tag{3.13}$$

Additionally, if the precoder of Eq. (3.5) is adopted, it holds that

$$d_n = \begin{cases} \Re\{b_{0,n}\} & \text{if } n \text{ odd} \\ \Im\{b_{0,n}\} & \text{if } n \text{ even} \end{cases}. \tag{3.14}$$

For illustration purposes, Fig. 3.6 shows the $c_0(t)$ pulse computed for the GMSK modulation with $BT = 0.25$ and $L = 5$.

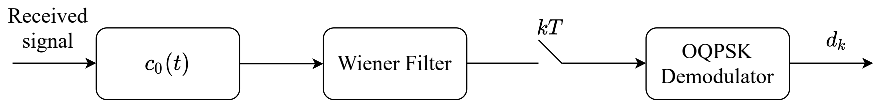

Figure 3.7: GMSK demodulator block diagram.

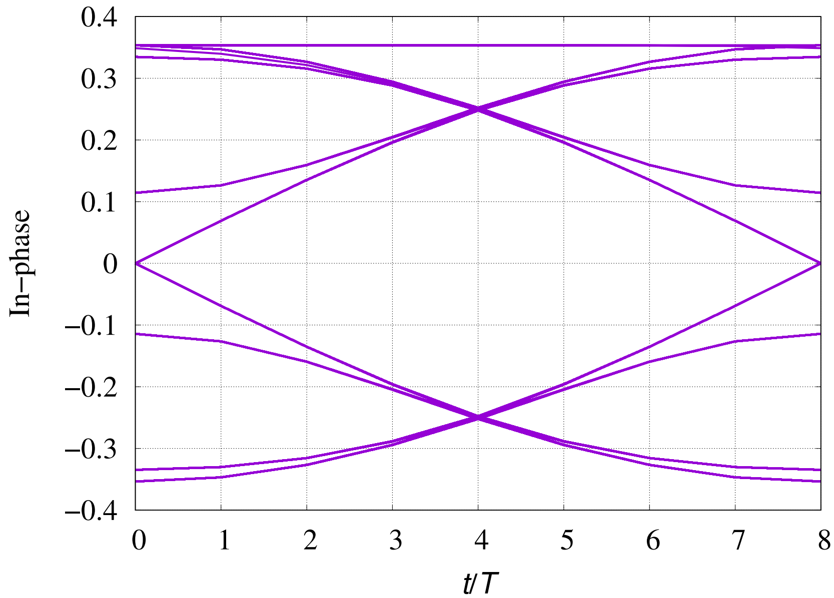

Figure 3.8: GMSK eye diagram ($BT = 0.5$).

3.1.3 Demodulator

Based on the Laurent approximation of (3.13) and the identity in (3.14), the GMSK demodulator can be implemented as the linear demodulator as depicted in Fig. 3.7.

Since it does not take into account higher-order $c_i(t)$ terms, the received signal will experience ISI, and thus a Wiener filter can be included for improving performance. Namely, CCSDS recommends [22] that a three-tap Wiener filter, of weights $w_0 = w_2 = -0859984.0$ and $w_1 = 0116342.1$ and inter-tap delay equal to $2T$, should be employed when $BT = 0.25$. Instead, for $BT = 0.5$, the Wiener filter can be avoided by accepting a small loss in the performance. The impact of ISI in the GMSK modulation is clearly seen in their eye diagrams, shown in Fig. 3.8 and 3.9. In fact, GMSK with $BT = 0.25$ has a much more closed eye than $BT = 0.5$.

Beyond the ISI introduced by the high order $c_i(t)$, the received signal experiences a linear ISI on the In-Phase (orthogonal) component that does not impact the performance. For simplicity, the discussion will be limited for a moment to the case of an MSK signal by fixing $h = 0.5$ and $L = 1$. Then, the received signal at the output of the front-end filter is

$$r(t, \mathbf{a}) = \sum_n \exp\left[\frac{j\pi}{2}\left(\sum_{m=-\infty}^{n} a_m\right)\right] u_0(t - nT)\,, \tag{3.15}$$

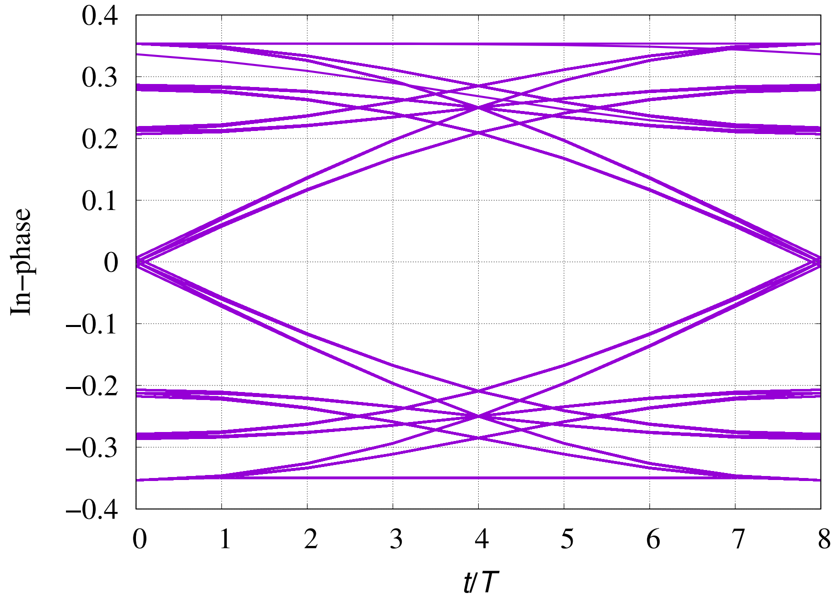

Figure 3.9: GMSK eye diagram ($BT = 0.25$).

where $u_0(t) = c_0(t) * c_0(-t)$ (where $*$ is the convolution operator), and

$$c_0(t) = \sin\left(\frac{\pi t}{2T}\right) . \tag{3.16}$$

To illustrate the effects of ISI, Fig. 3.10 shows the superposition of two adjacent $u_0(t)$ pulses. From the figure, it can be seen that there is an orthogonal ISI that can take values in $\{-0.62, 0, 0.62\}$, depending on the sign of the adjacent symbols. This is shown very well in the scattering diagram of the received MSK symbols of Fig. 3.11, where symbols' Q-component can be ± 1 (thus providing the original bit sequence) while the I-component continuously varies.

In a similar way, GMSK experiences ISI on both the I/Q components, but only the latter impacts the performance. That is well shown in Fig. 3.12, and 3.13, which provide the scattering diagram of the received GMSK symbols for $BT = 0.25$ and 0.5, respectively.

Given the similarity between GMSK and linear modulations, the ideal BER of a GMSK signal is provided by the BPSK BER closed formula, that reads

$$P_b = \frac{1}{2}\text{erfc}\left(\sqrt{\frac{E_b}{N_0}}\right) , \tag{3.17}$$

where E_b is the energy per bit.
In reality, because of the residual ISI, the GMSK will experience slightly worse error performance. Fig. 3.14 shows the GMSK BER with $BT = 0.25$ and 0.5 in comparison with (3.17), computed using Monte Carlo simulations. As expected, it can be seen that a GMSK with $BT = 0.5$ has an

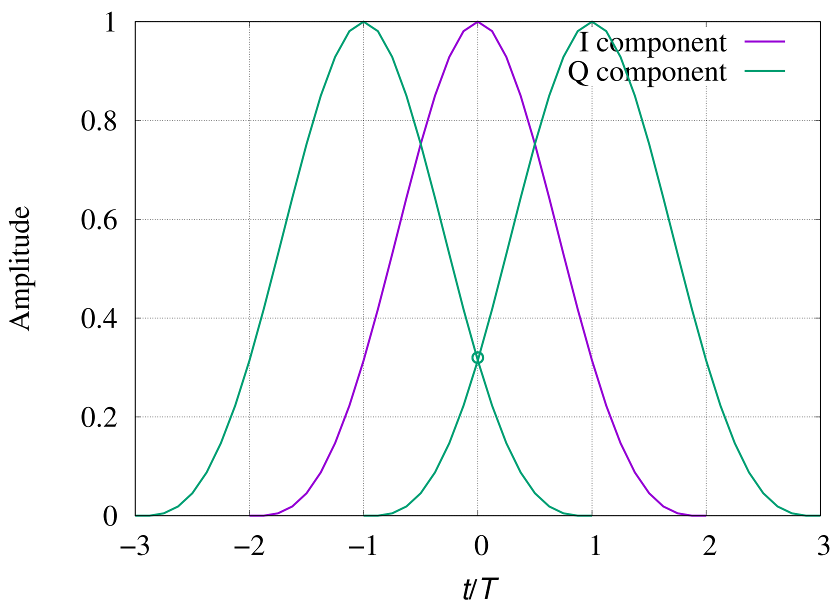

Figure 3.10: Adjacent MSK symbols at receiver side.

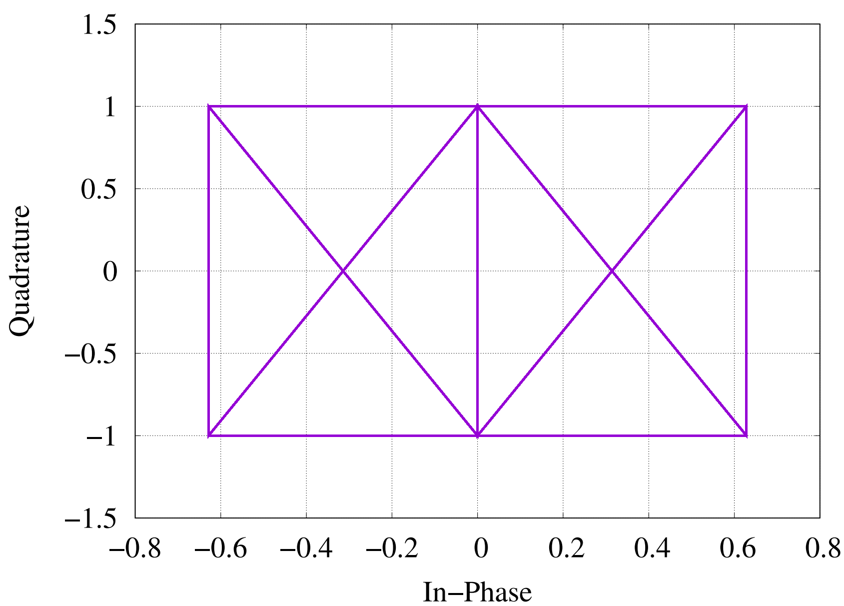

Figure 3.11: Scattering diagram at the receiving end for MSK modulation.

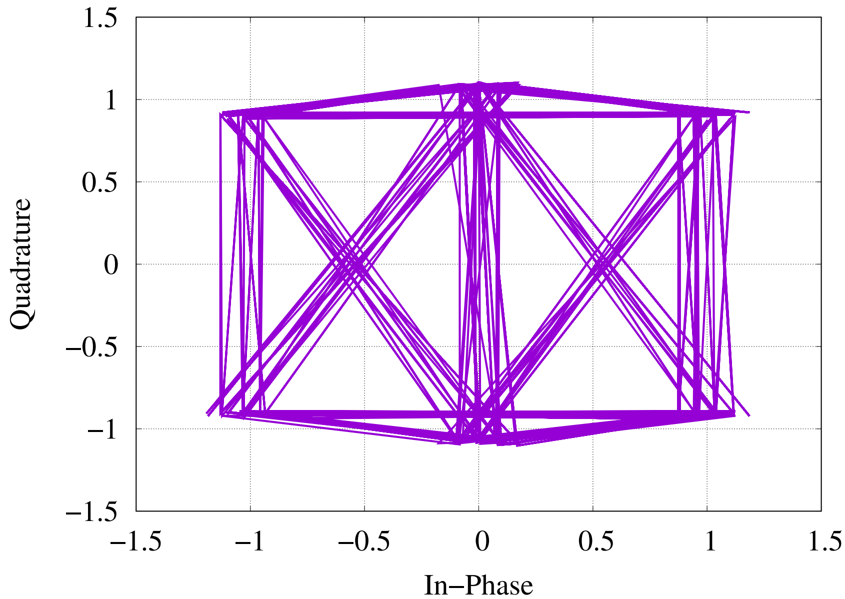

Figure 3.12: Scattering diagram at the receiving end for GMSK ($BT = 0.25$) modulation.

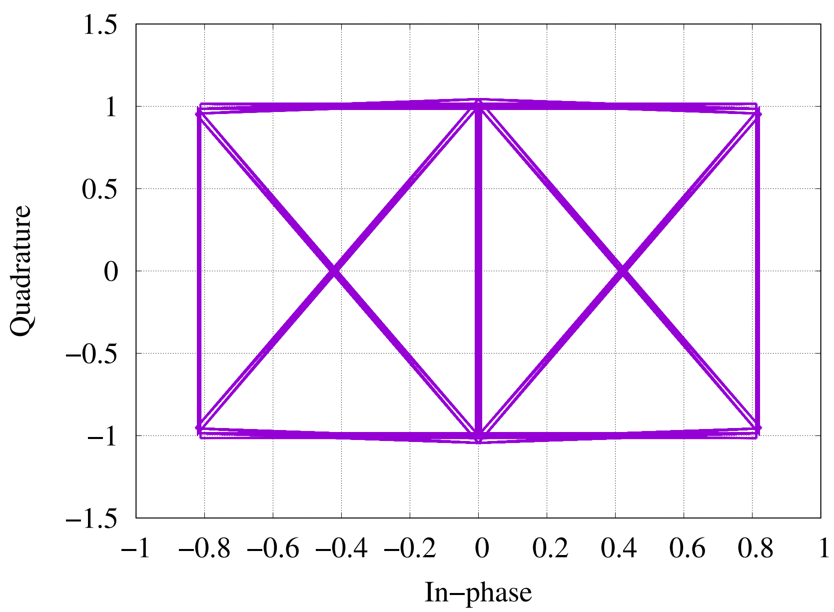

Figure 3.13: Scattering diagram at the receiving end for GMSK ($BT = 0.5$) modulation.

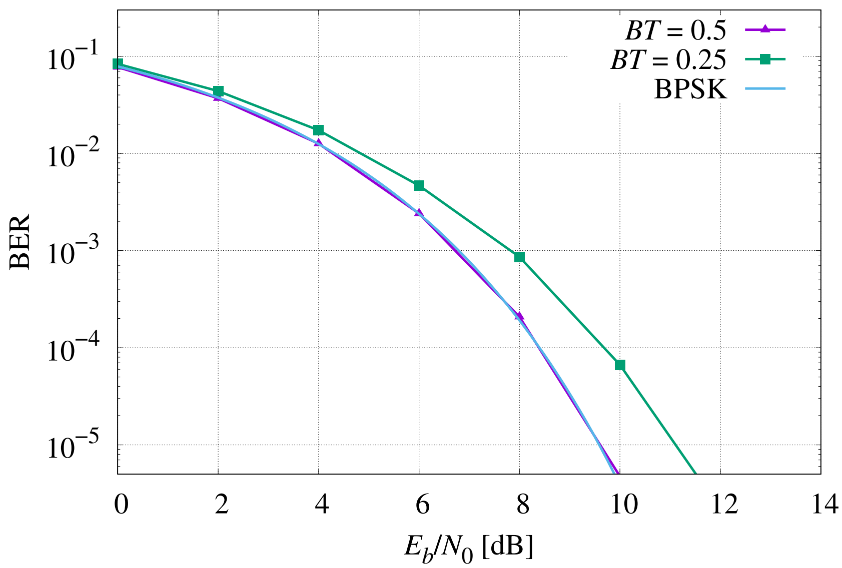

Figure 3.14: BER curve for GMSK and BPSK modulation.

almost ideal BER, while, there is a loss of about 2 dB for $BT = 0.25$. This loss can be decreased by means of the Wiener filter recommended by CCSDS: Fig. 3.15 provides a comparison of the BER curves with and without Wiener filter. It can be seen that about 1 dB is gained.

3.2 GMSK Telemetry and PN Ranging

Having discussed the PN Ranging signal characteristics in Chapter 2 and the GMSK signal properties in the previous section, their combination is now addressed. This section aims at presenting the validation results of the GMSK-PN Ranging system and at being a reference for the novel SCCC-PN Ranging system of Chapter 4. The simultaneous transmission scheme for the PN Ranging and the GMSK-modulated telemetry is reported in Fig. 3.16. This last has been obtained by combining the transmission systems of the two, described in Section 2.3 and 3.1, respectively. The output signal is defined as

$$\exp(j\Phi_{TM}(t, \mathbf{a}) \cdot \exp(j\Phi_{RG}(t - \tau_{RG})) \tag{3.18}$$

where, $\Phi_{TM}(t, \mathbf{a})$ and $\Phi_{RG}(t)$ refer to the telemetry and ranging modulated phase shift, defined in (3.3) and (2.3), respectively [17], and τ_{RG} is the timing delay estimated through the CTL.

3.2.1 Spectral Occupancy

To address how the ranging signal affects the GMSK-modulated telemetry bandwidth, the power spectral density has been analyzed. The power spectrum estimations involved different modulation indexes and chip-rate-to-telemetry-symbol-rate ($\frac{R_{RG}}{R_{TM}}$) ratios for the T2B and the T4B

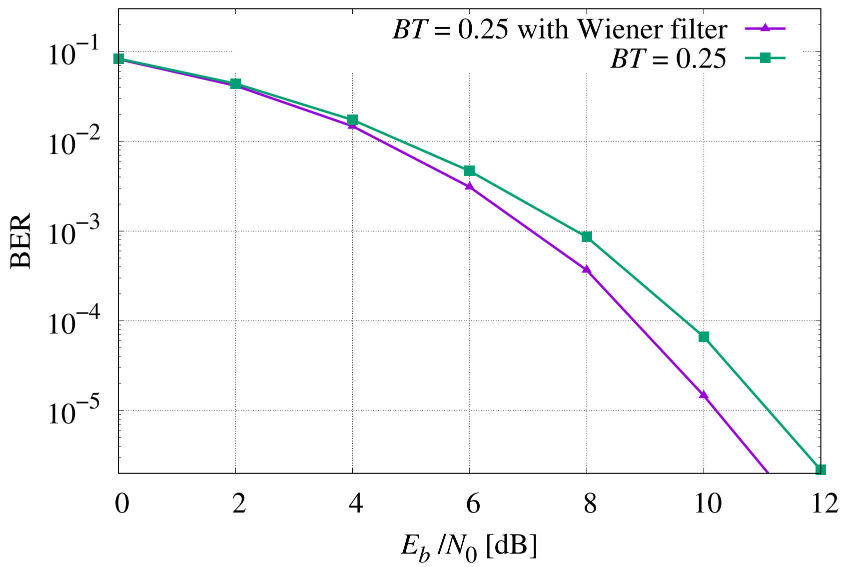

Figure 3.15: Comparison between BER obtained with and without Wiener filter for GMSK with $BT = 0.25$.

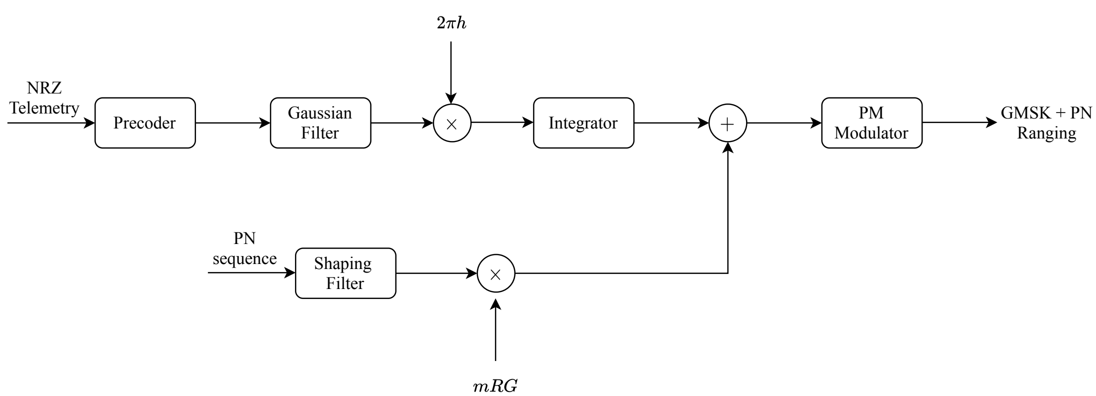

Figure 3.16: Block diagram of GMSK-PN Ranging system transmitter.

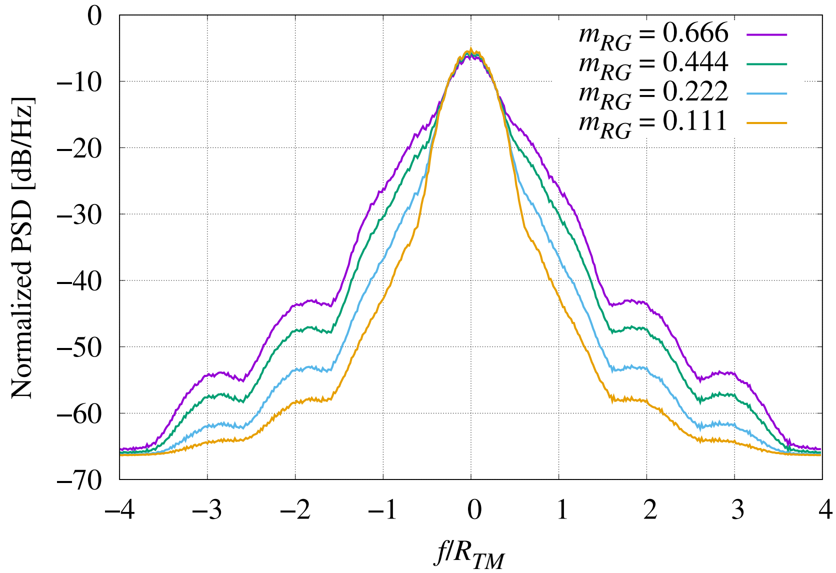

Figure 3.17: Power spectral density of GMSK ($BT = 0.25$), $R_{RG} \approx R_{TM}$ and T2B PN code.

scheme using sinusoidal-shaped chips. Additionally, the 99-percent power bandwidth has been evaluated to investigate how the ranging signal impacts the spectral occupancy. Because of GMSK modulation's constant envelope property, the channel can be considered linear, and thus, the following results have been obtained using computer simulation over an AWGN channel.

Fig. 3.17-3.24 show the PSD of the GMSK signal combined with PN Ranging for different modulation indexes and by using the T2B and T4B PN codes. Since the modulation index m_{RG} determines which component has greater power, it can be seen that the higher m_{RG}, the larger the slice of power devoted to the ranging signal rather than to the telemetry signal. Therefore, the secondary lobes are more pronounced, leading to a spectrum broadening and a distortion of the GMSK signal. Tab. 3.1 and 3.2 report the 99-percent normalized bandwidth, computed with respect to the telemetry channel symbol rate R_{TM}. The results for $\frac{R_{RG}}{R_{TM}} \approx 1$ have been reported solely to validate the measurements with those in [17]. The spectral performance of the GMSK-PN Ranging system at the chip-rate-to-telemetry-rate of ≈ 1 and $\approx \frac{1}{3}$ have been compared. For the last ratio, a chip rate $R_{RG} = 3$ Mchip/s and a telemetry channel symbol rate $R_{TM} = 8.4$ Msymbol/s have been simulated. It can be observed that, rather than $\frac{R_{RG}}{R_{TM}} \approx 1$, for $\frac{R_{RG}}{R_{TM}} \approx \frac{1}{3}$ the ranging has a lower impact: the bandwidth of the GMSK-modulated telemetry predominates on the ranging signal's one. Indeed, the 99-percent power bandwidth does not grow as much as it does for $\frac{R_{RG}}{R_{TM}} \approx 1$ when the modulation index increases.

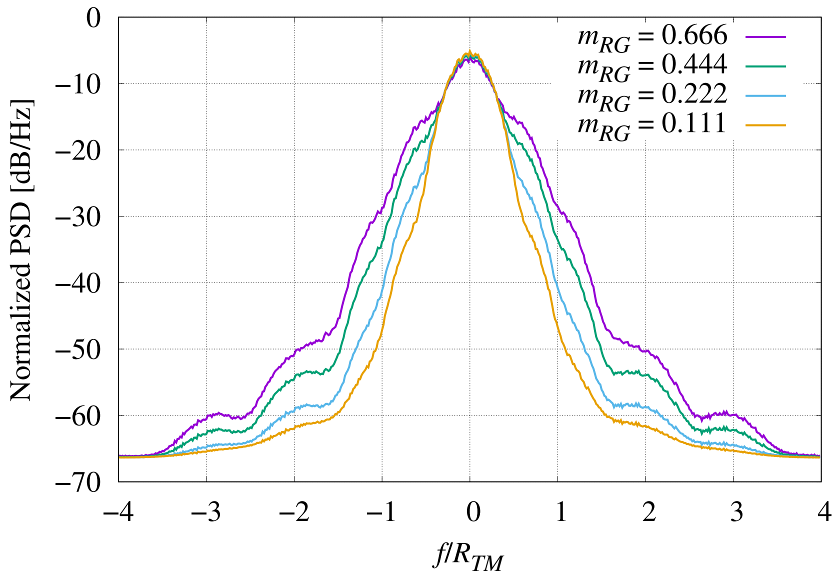

Figure 3.18: Power spectral density of GMSK ($BT = 0.25$), $R_{RG} \approx R_{TM}$ and T4B PN code.

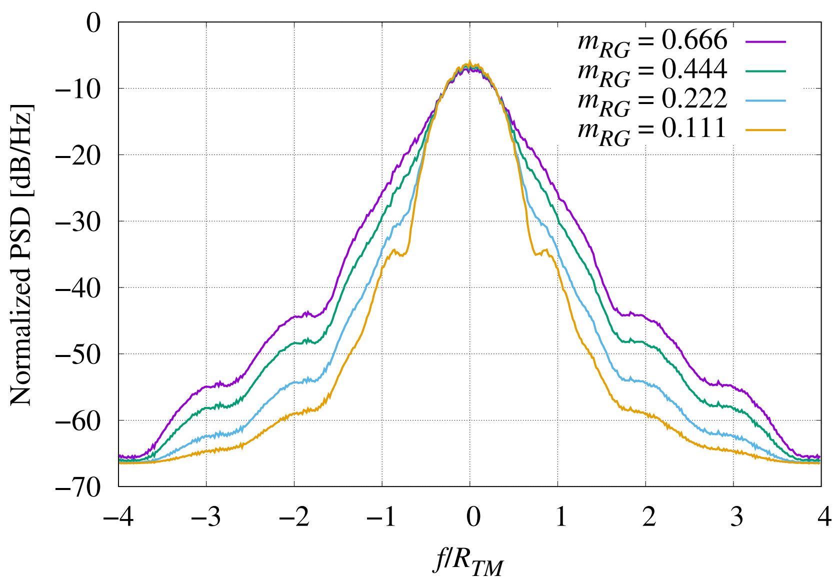

Figure 3.19: Power spectral density of GMSK ($BT = 0.5$), $R_{RG} \approx R_{TM}$ and T2B PN code.

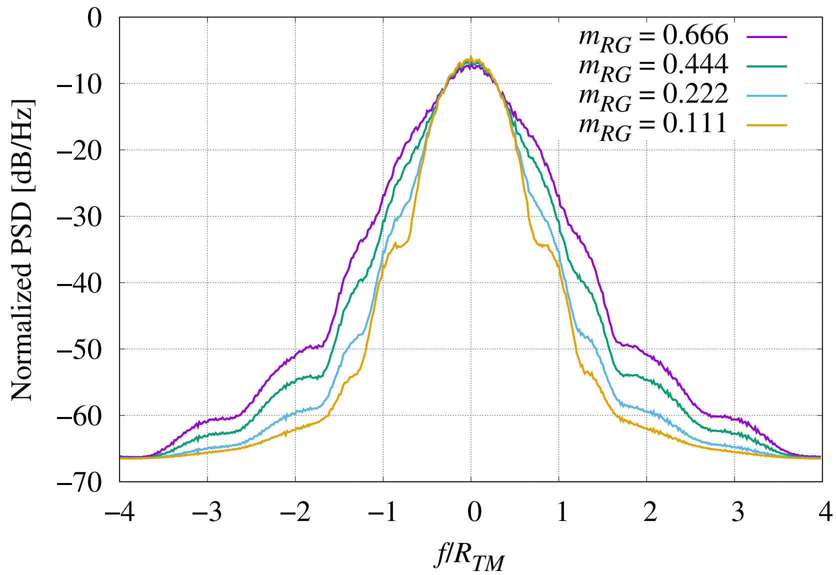

Figure 3.20: Power spectral density of GMSK ($BT = 0.5$), $R_{RG} \approx R_{TM}$ and T4B PN code.

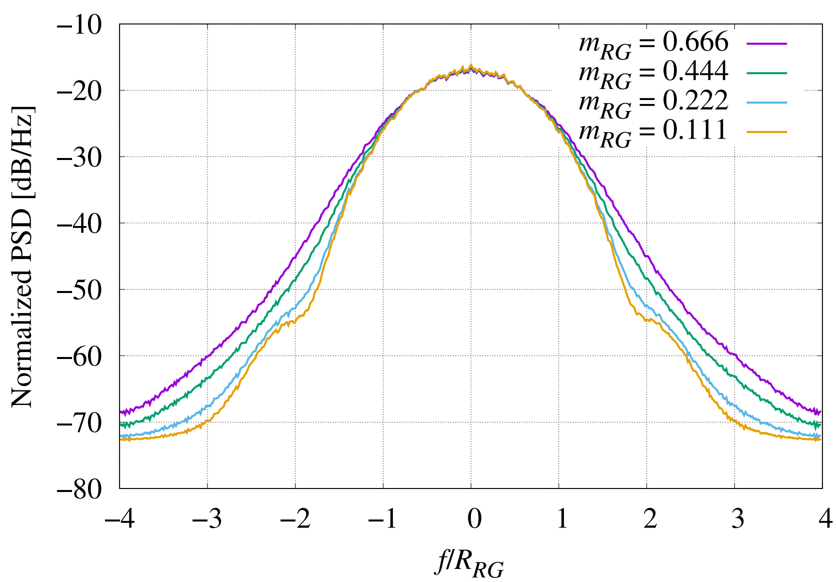

Figure 3.21: Power spectral density of GMSK ($BT = 0.25$), $R_{RG} \approx \frac{1}{3}\ R_{TM}$ and T2B PN code.

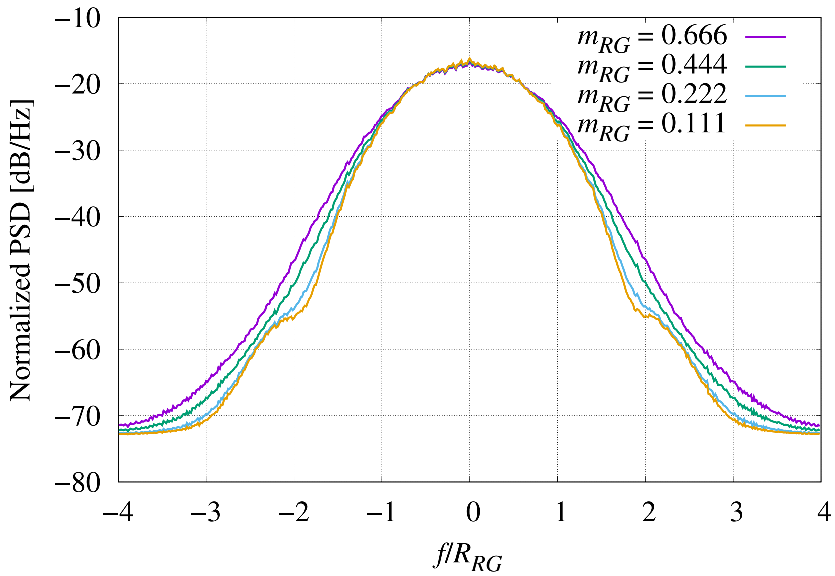

Figure 3.22: Power spectral density of GMSK ($BT = 0.25$), $R_{RG} \approx \frac{1}{3}\ R_{TM}$ and T4B PN code.

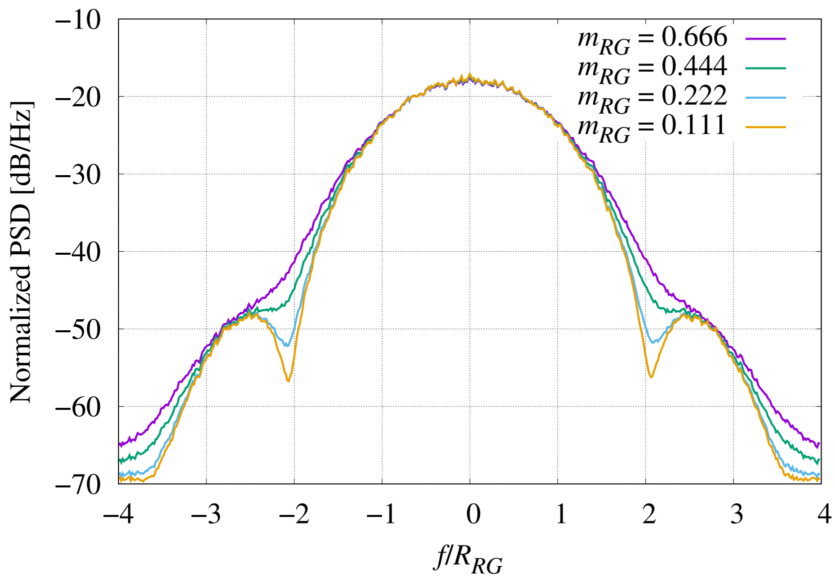

Figure 3.23: Power spectral density of GMSK ($BT = 0.5$), $R_{RG} \approx \frac{1}{3}\ R_{TM}$ and T2B PN code.

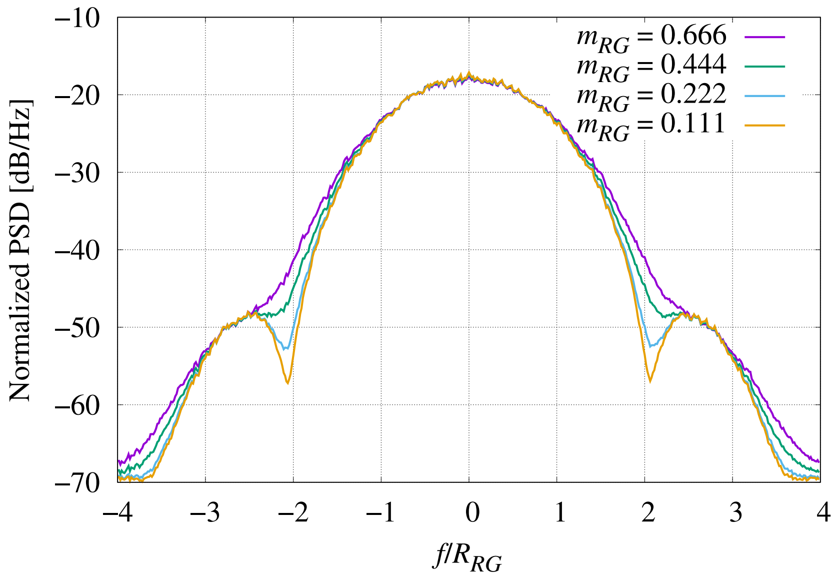

Figure 3.24: Power spectral density of GMSK ($BT = 0.5$), $R_{RG} \approx \frac{1}{3}\ R_{TM}$ and T4B PN code.

m_{RG}	$BT = 0.25$		$BT = 0.5$	
	T2B	T4B	T2B	T4B
0.111	0.89	0.91	1.06	1.06
0.222	1.06	1.09	1.17	1.19
0.444	1.53	1.47	1.59	1.55
0.666	1.86	1.69	1.94	1.78

Table 3.1: AWGN 99% bandwidth for $R_{RG} \approx R_{TM}$ with GMSK-modulated telemetry.

m_{RG}	$BT = 0.25$		$BT = 0.5$	
	T2B	T4B	T2B	T4B
0.111	0.86	0.86	1.03	1.03
0.222	0.87	0.87	1.04	1.04
0.444	0.93	0.92	1.08	1.08
0.666	1	0.98	1.15	1.14

Table 3.2: AWGN 99% bandwidth for $R_{RG} \approx \frac{1}{3}\ R_{TM}$ with GMSK-modulated telemetry.

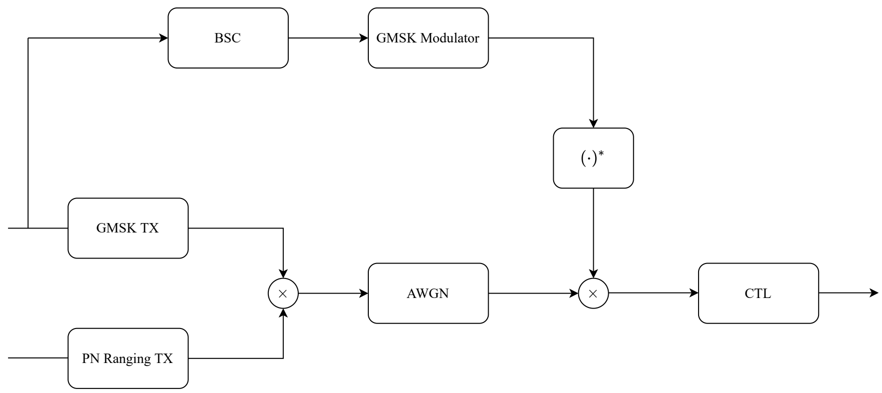

Figure 3.25: Block diagram of GMSK-PN Ranging system with open-loop receiver.

3.2.2 Receiver Ranging Performance

As a first analysis to evaluate the GMSK-PN Ranging system and, in particular, its CTL performance, a genie-aided scheme, with a block diagram as shown in Fig. 3.25, was implemented. Namely, the receiver has been simulated in open-loop, meaning that, instead of using the received signal to recover the telemetry symbols, their detection has been emulated in accordance to the bit error probability of BPSK modulation (3.17), on top of which an additional loss, L_{GMSK}, has been considered to account for the introduced ISI by GMSK modulation and other impairments. At the receiver end, the complex conjugate of the telemetry symbols, thus obtained, is multiplied by the received signal to extract the PN chips to be input to the CTL. The latter has been tuned using $\gamma = 0.01$ that, by recalling the relationship that binds γ and B_L expressed in (2.10) and knowing that $T_c = \frac{1}{R_{RG}} = 3$ Mchip/s, is equivalent to a loop bandwidth is 15 kHz.

In ideal conditions, the telemetry symbols are entirely canceled from the received signal, leading to an ideal recovery of the chips, besides the AWGN introduced by the channel. Fig. 3.26 reveals how in ideal conditions the GMSK-PN Ranging system's normalized timing jitter perfectly matches the theoretical one.[1]. Conversely, the simulation of a non ideal telemetry cancellation (Fig. 3.27) shows the normalized timing jitter deviating from the theoretical curve for small values of $\frac{P}{N_0 B_L}$ but, as the latter grows, it asymptotically converges to the theoretical one. What might be interesting to notice is that the CTL performance is quite resilient to the additional loss. This behavior can be easily explained by looking at Fig. 3.28 in which it is clear that, for the reference values of $\frac{P}{N_0 B_L}$ ratios, the BER is already below 10^{-3}, and thus the timing jitter is just noise limited.

3.2.3 End-to-end Performance

At this point, the whole transmission and reception chain has been implemented and simulated to estimate the performance of the GMSK-PN Ranging receiver. According to [17], the receiver has been implemented as in Fig. 3.29 using a closed-loop scheme in which the signal input to

[1] For the sake of completeness Fig. 3.26 presents the results for both, the sinusoidal and the square chip shaping pulse, but future analysis will regard the sinusoidal only.

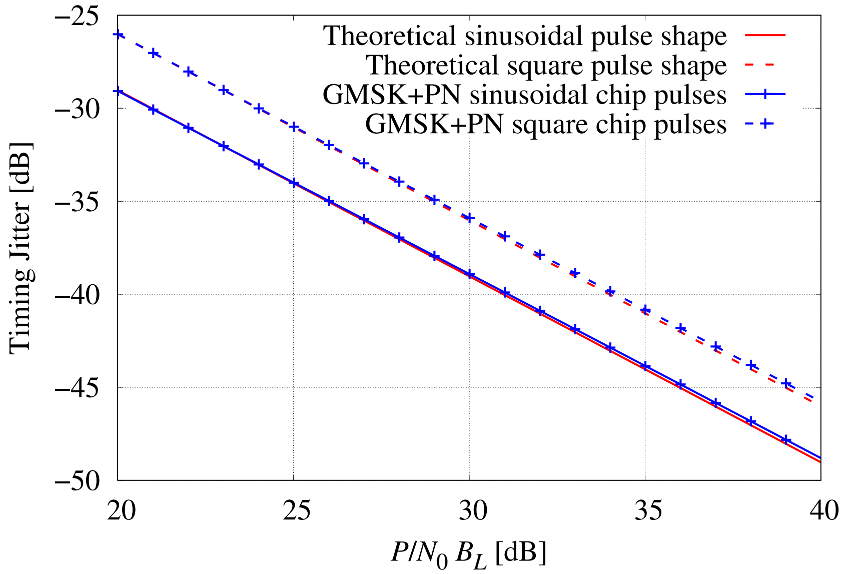

Figure 3.26: Timing jitter $\widetilde{\sigma}_{\tau}^{2}$ of GMSK-PN Ranging system under the ideal telemetry cancellation condition compared to the theoretical curves.

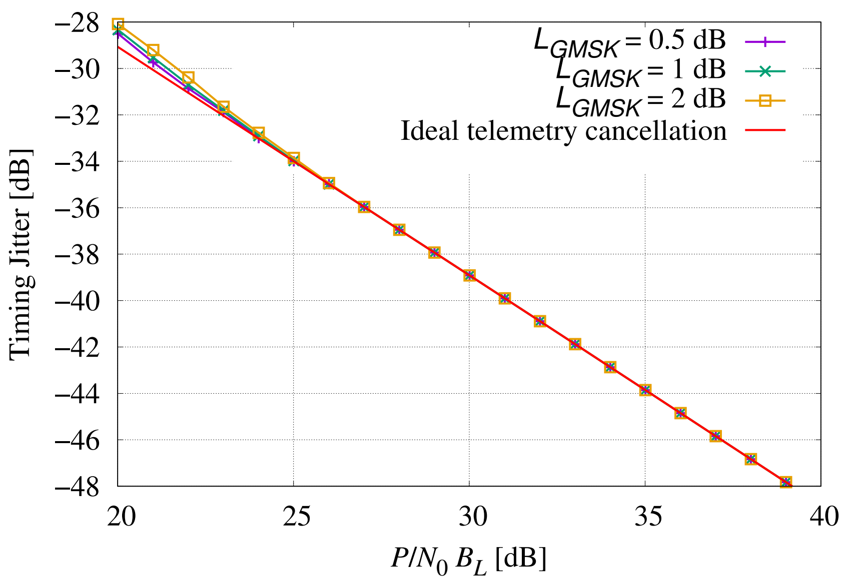

Figure 3.27: Timing jitter $\widetilde{\sigma}_{\tau}^{2}$ comparison with ideal telemetry cancellation and different noise levels for GMSK-modulated telemetry.

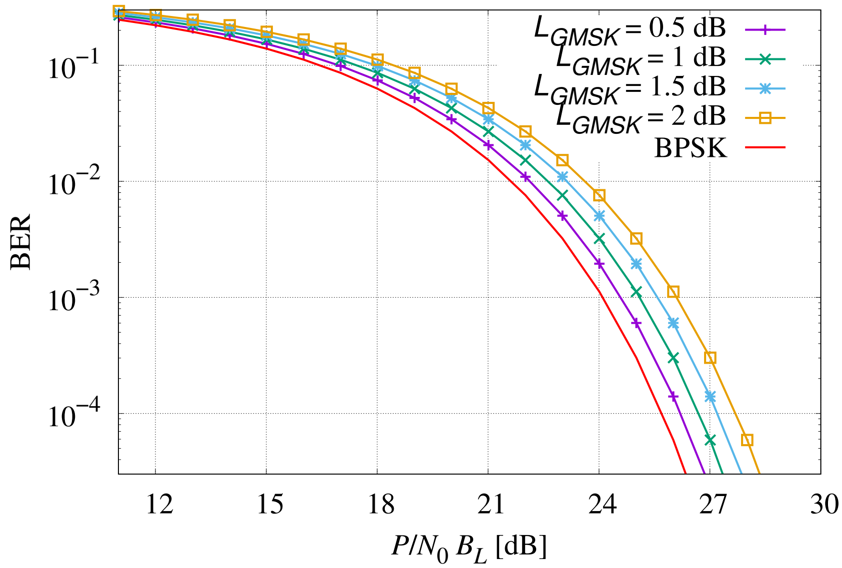

Figure 3.28: BER with additional loss with respect to BPSK.

the receiver is removed from the ranging component by multiplying it for the complex conjugate of the ranging sequence. This last can be locally generated, being known except (at least at the beginning) from the correct time delay. The telemetry stream thus obtained is demodulated and re-modulated to reproduce the sequence of symbols and, with it, its complex conjugate necessary to remove the telemetry component from the received signal. Then, the ranging sequence hence extracted is input to the CTL, which, on its own, feeds the PN Ranging local generator with the estimated timing delay.

On the telemetry side, the numerical results showed a perfect matching to the BER curve of a GMSK ($BT = 0.25$) modulated signal, as can be seen in Fig. 3.30.

Similarly, results reported in Fig. 3.31 proved that the CTL performed, apart from an initial separation due to the low E_b/N_0 involved, as the ideal case. Thus, the performance of the closed-loop receiver turned out to be even better than that predicted by the open-loop one.

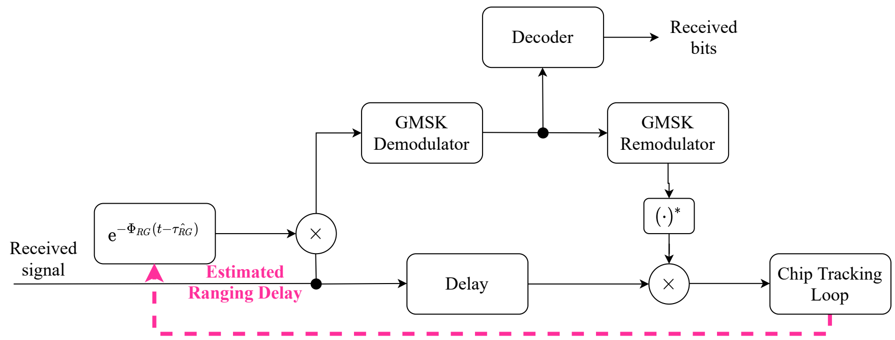

Figure 3.29: GMSK-PN Ranging closed-loop receiver.

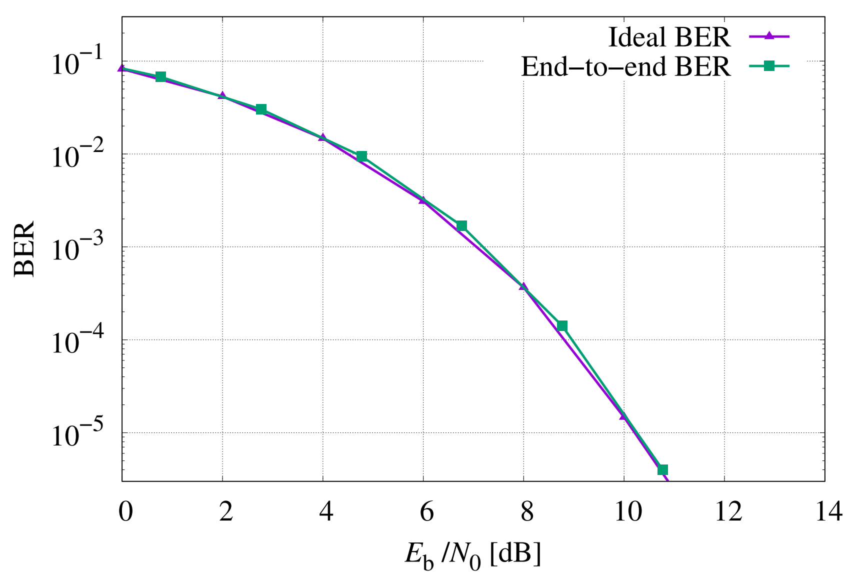

Figure 3.30: BER resulting from the ranging cancellation of a closed-loop receiver and BER of a GMSK only telemetry signal.

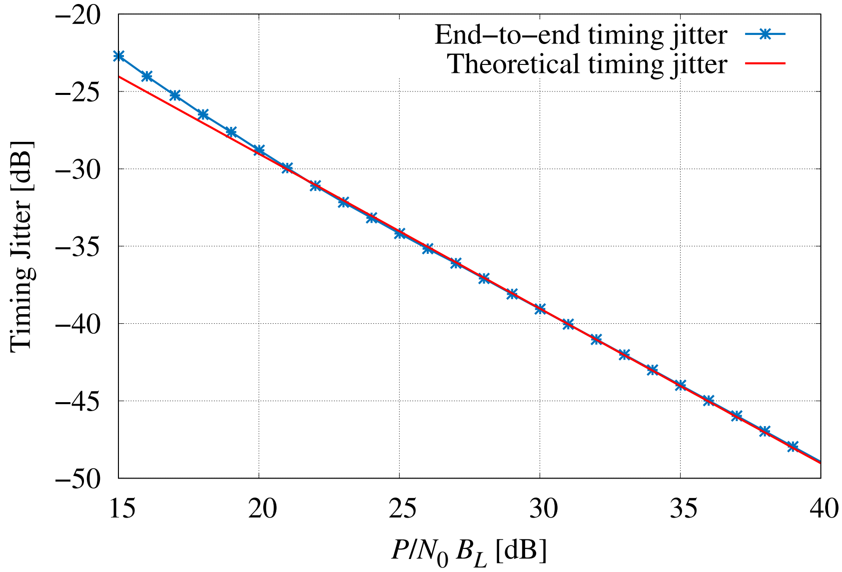

Figure 3.31: End-to-end timing jitter $\widetilde{\sigma}_\tau^2$ versus theoretical one.

Chapter 4

PN Ranging and SCCC

This chapter presents the feasibility study of the combination of the ranging system with high-order modulation formats. In particular, these modulations are those included in the CCSDS standard 131.2 [10], usually known in the TT&C community as SCCC. This name is justified by the turbo-like coding/modulation scheme based on the use of a Serial Concatenated Convolutional Code (SCCC) [23]. However, in this thesis, the term "SCCC" refers solely to uncoded modulation formats. The standard covers several modulations, i.e., QPSK, 8-PSK, 16-APSK, 32-APSK, and 64-APSK, and several coding rates. Tab. 4.1 lists the SNR thresholds necessary to achieve a Codeword Error Rate (CER) of 10^{-4}, along with the spectral efficiency and the degradation losses for all the 27 adaptive modulation and coding (ACM) formats of the standard [5]. What makes the proposed SCCC-PN Ranging system attractive, is the efficient use of the available bandwidth. Additionally, if the performance of this novel system proved to be comparable to that of the classical approach of using GMSK, the data rate would be at least doubled.

It is assumed that the simultaneous transmission of the SCCC-modulated telemetry and the PN Ranging signal follows the same scheme described for the GMSK-PN Ranging system and depicted in Fig. 4.1. The ranging signal $\Phi_{RG}(t)$ (as expressed in (2.3)) is phase modulated as

$$r_{RG}(t) = \exp\left(j\Phi_{RG}(t)\right) , \tag{4.1}$$

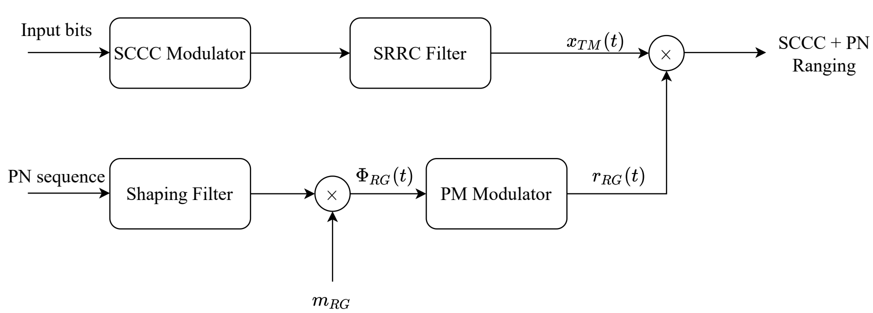

Figure 4.1: Block diagram of SCCC-PN Ranging system.

and it holds $|r_{RG}(t)|^2 = 1$.
Then, the transmitted signal is obtained as the (complex base-band) product of $r_{RG}(t)$ with the SCCC telemetry signal $x_{TM}(t)$. For sake of clarity, the telemetry signal is considered having unitary power.

At the receiving end, the received signal is

$$y(t) = x_{TM}(t)r_{RG}(t) + w(t)\,, \tag{4.2}$$

where $w(t)$ is white Gaussian noise having power spectral density equal to N_0. The receiver simultaneously demodulates telemetry symbols and tracks the ranging sequence. To extract the telemetry stream input to demodulator, the ranging sequence is canceled out from the received signal by a complex multiplication

$$\begin{aligned} y(t)r^*_{RG}(t) &= x_{TM}(t)|r_{RG}(t)|^2 + w(t)r^*_{RG}(t) &(4.3)\\ &= x_{TM}(t) + w^{''}(t)\,, &(4.4)\end{aligned}$$

where it is easy to see that, since $r_{RG}(t)$ is a phasor, $w^{''}(t) = w(t)r^*_{RG}(t)$ is still a white Gaussian random process.

A similar procedure can be followed to recover the PN chip sequence $r_{RG}(t)$. In fact, if the received signal is multiplied by the complex conjugate of the telemetry signal, it results that

$$\begin{aligned} y(t)x^*_{TM}(t) &= r_{RG}(t)|x_{TM}(t)|^2 + w(t)x^*_{TM}(t) &(4.5)\\ &= r_{RG}(t)|x_{TM}(t)|^2 + w^{'}(t)\,, &(4.6)\end{aligned}$$

where $w^{'}(t) = w(t)x^*_{TM}(t)$ is, as shown in Section 4.1, still a white process.

Since the PSK/APSK modulations are Square Root Raised Cosine (SRRC) filtered [10], $|x_{TM}(t)|^2$ is different from 1, hence a perfect cancellation cannot be achieved. However, it holds that $\mathbb{E}[|x_{TM}(t)|^2] = 1$, and a sub-optimal cancellation can be performed by averaging the samples. Consequently, a possible design of receiver doing simultaneous demodulation of SCCC and tracking of PN Ranging is proposed in Fig. 4.2. The latter has been derived from the GMSK-PN Ranging receiver (Section 3.2), in which the GMSK demodulator and re-modulator have been replaced with the SCCC components. In line with the already described system, the receiver iteratively performs the ranging and telemetry signals' cancellation over the received stream in a closed-loop. However, in this case the CTL bandwidth (B_L) is tuned by taking into account that low values of B_L allow better averaging over the time-varying envelope of $x_{TM}(t)$, thereby approaching the optimal telemetry cancellation.

The remainder of this chapter is organized as follows: Section 4.1 and Section 4.2 analyze the performance of the SCCC modulations with PN Ranging. Namely, the spectral occupancy at the transmitter is provided, and the PN Ranging jitter performance is computed by a genie-aided receiver scheme. These results are then compared with those obtained for GMSK in Section 3.2. Finally, Section 4.3 evaluates the end-to-end performance of the full receiver and draws the conclusions.

4.1 PSK and PN Ranging

4.1.1 Spectral Occupancy

This section analyzes the spectral occupancy, as the 99-percent power bandwidth, of PSK modulations with PN ranging, shown in Tab. 4.2, computed with respect to R_{TM}, and under AWGN

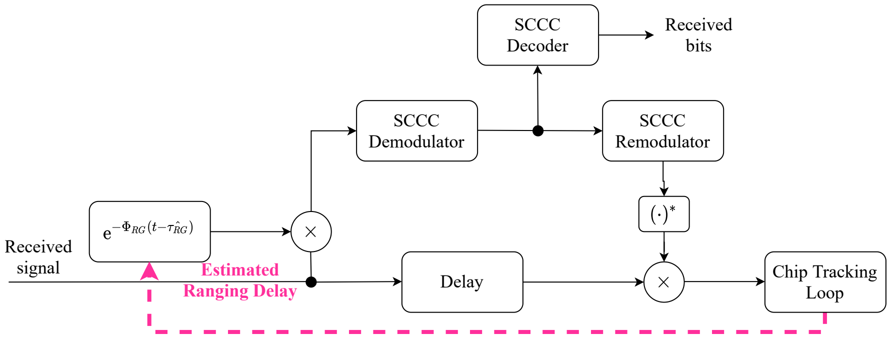

Figure 4.2: SCCC-PN Ranging closed-loop receiver.

	ACM	E_s/N_0	E_b/N_0	TD [dB]	Efficiency	Bandwidth
QPSK	1	-0.58	0.90	0.98	0.71	$1.29 \cdot \mathrm{R}_{chs}$
	2	0.42	1.08	0.94	0.86	$1.29 \cdot \mathrm{R}_{chs}$
	3	1.60	1.44	0.94	1.04	$1.29 \cdot \mathrm{R}_{chs}$
	4	2.71	1.87	0.90	1.21	$1.29 \cdot \mathrm{R}_{chs}$
	5	3.83	2.39	0.91	1.39	$1.29 \cdot \mathrm{R}_{chs}$
	6	5.42	3.30	0.96	1.63	$1.29 \cdot \mathrm{R}_{chs}$
8-PSK	7	3.91	2.41	0.95	1.39	$1.29 \cdot \mathrm{R}_{chs}$
	8	5.10	3.00	0.99	1.63	$1.29 \cdot \mathrm{R}_{chs}$
	9	6.25	3.63	1.01	1.84	$1.29 \cdot \mathrm{R}_{chs}$
	10	7.75	4.53	1.11	1.84	$1.27 \cdot \mathrm{R}_{chs}$
	11	9.21	5.46	1.30	2.37	$1.27 \cdot \mathrm{R}_{chs}$
	12	10.90	6.69	1.65	2.46	$1.27 \cdot \mathrm{R}_{chs}$
16-APSK	13	8.18	4.45	2.78	2.37	$1.24 \cdot \mathrm{R}_{chs}$
	14	9.24	5.03	2.97	2.37	$1.24 \cdot \mathrm{R}_{chs}$
	15	10.34	5.67	3.30	2.90	$1.23 \cdot \mathrm{R}_{chs}$
	16	11.55	6.50	3.76	3.20	$1.23 \cdot \mathrm{R}_{chs}$
	17	13.02	7.58	4.43	3.50	$1.21 \cdot \mathrm{R}_{chs}$
32-APSK	18	11.46	7.58	5.43	3.20	$1.20 \cdot \mathrm{R}_{chs}$
	19	12.52	7.08	5.75	3.50	$1.20 \cdot \mathrm{R}_{chs}$
	20	13.49	7.69	6.19	3.82	$1.19 \cdot \mathrm{R}_{chs}$
	21	14.62	8.49	6.69	4.12	$1.18 \cdot \mathrm{R}_{chs}$
	22	16.04	9.61	7.37	4.44	$1.18 \cdot \mathrm{R}_{chs}$
64-APSK	23	14.73	8.56	6.64	4.12	$1.18 \cdot \mathrm{R}_{chs}$
	24	15.74	9.27	7.19	4.44	$1.18 \cdot \mathrm{R}_{chs}$
	25	16.83	10.07	7.92	4.77	$1.17 \cdot \mathrm{R}_{chs}$
	26	17.85	10.83	8.77	5.06	$1.17 \cdot \mathrm{R}_{chs}$
	27	19.10	11.78	9.84	5.39	$1.17 \cdot \mathrm{R}_{chs}$

Table 4.1: SNR thresholds for CER=10^{-4}, corresponding total degradation (TD) and occupied bandwidth, achieved by the SCCC modulation and coding formats with SRRC roll-off 0.35 in end-to-end simulations and without pre-distortion (as reported in [5]).

m_{RG}	QPSK		8-PSK	
	T2B	T4B	T2B	T4B
0.111	1.16	1.16	1.16	1.16
0.222	1.20	1.20	1.20	1.20
0.444	1.52	1.52	1.50	1.52
0.666	1.74	1.70	1.74	1.70

Table 4.2: AWGN 99% bandwidth for PSK-modulated telemetry (SRRC with roll-off 0.35).

m_{RG}	QPSK		8-PSK	
	T2B	T4B	T2B	T4B
0.111	1.25	1.25	1.25	1.25
0.222	1.29	1.29	1.29	1.29
0.444	1.38	1.43	1.38	1.43
0.666	1.47	1.47	1.47	1.47

Table 4.3: TWTA 99% bandwidth for PSK-modulated telemetry (SRRC with roll-off 0.35).

conditions. For a fair comparison, it is highlighted that the telemetry channel symbol rate, against which the 99-percent power bandwidth has been referred, is halved with respect to the GMSK case. In fact, for the M-PSK modulations the telemetry channel symbol rate and the chip rate have been set to $R_{TM} = 4.2$ Msymbol/s and $R_{RG} = 3$ Mchip/s, respectively.

The power spectral densities, referred to the chip rate R_{RG}, for QPSK and 8-PSK, and for both the code schemes (T2B and T4B), are reported in Fig. 4.3, 4.4,4.5,4.6. It can be seen that, as for GMSK-modulated telemetry, the spectral occupancy is independent of the code scheme employed and, as expected, QPSK and 8-PSK have the same spectral occupancy. Additionally, the PSK modulations show improved spectral efficiency with respect to GMSK, as reported in Tab. 3.1 and 3.2.

On the other hand, conversely to GMSK, PSK are non-constant envelope modulations and cannot exploit power amplifiers up to saturation because of distortion. Hence, the occupied bandwidth in presence of nonlinear effects was preliminary analyzed by repeating simulation measurements applying a Traveling Wave Tube Amplifier (TWTA) and an elliptical filter (as those reported in [5]) to compensate for the spectrum broadening after the power amplifier. The bandwidth under non-linear conditions was computed as 99-percent of the signal power at the output of a power amplifier, with operating point Input Back-Off (IBO) equal to 0 dB, and to which corresponded an almost identical Output Back-Off (OBO). The resulting spectra are shown in Fig. 4.7 and 4.8 and apply only to the T4B scheme. It can be seen that the spectral efficiency is almost independent of the ranging modulation index (m_{RG}). However, for large values of m_{RG} the losses in the CTL will presumably increase due to the RF filter, a point that will be further explored in future work.

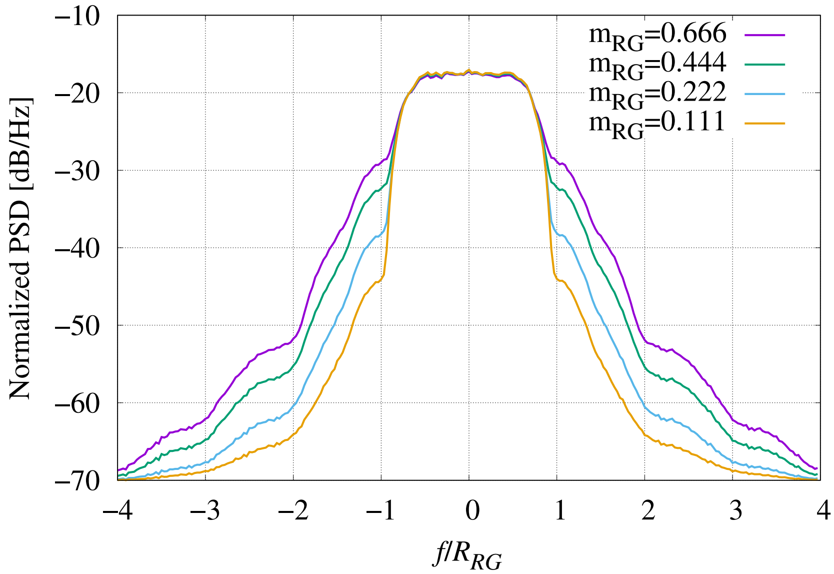

Figure 4.3: Power spectral density of QPSK (SRRC with roll-off 0.35) for T2B PN code under AWGN.

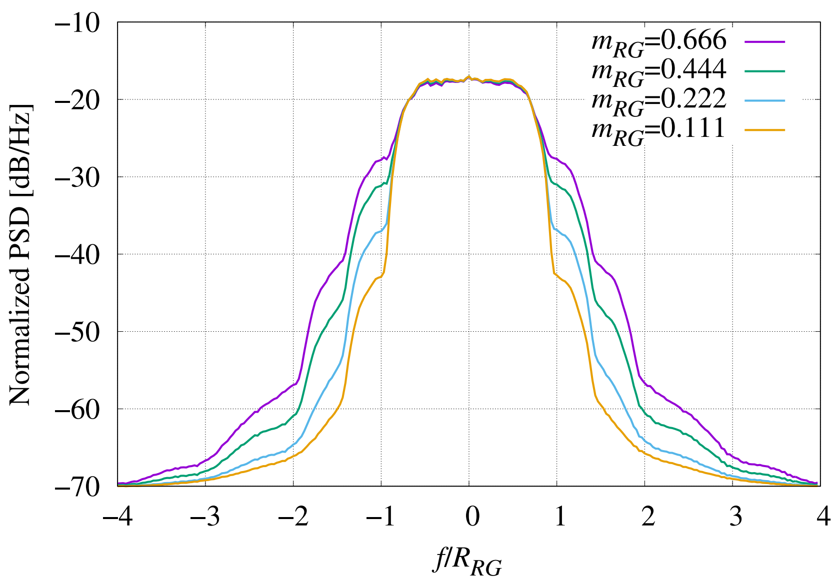

Figure 4.4: Power spectral density of QPSK (SRRC with roll-off 0.35) for T4B PN code under AWGN.

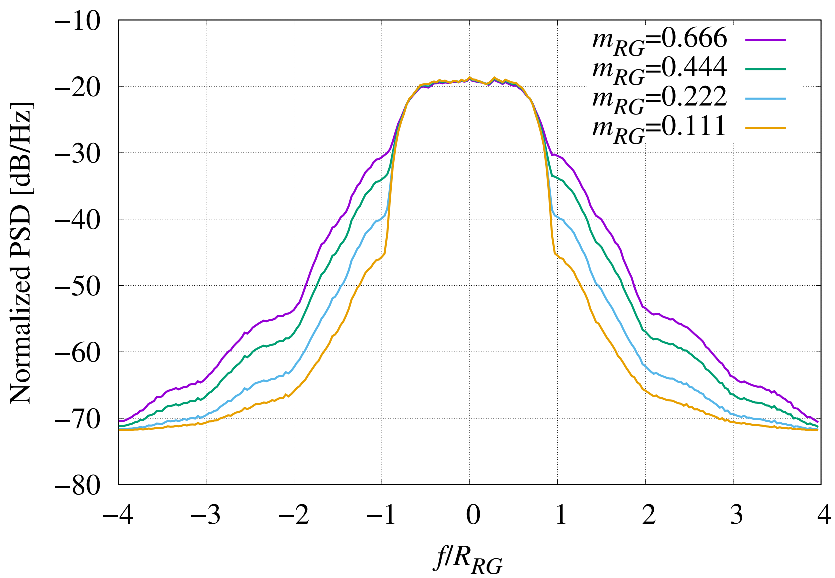

Figure 4.5: Power spectral density of 8-PSK (SRRC with roll-off 0.35) for T2B PN code under AWGN.

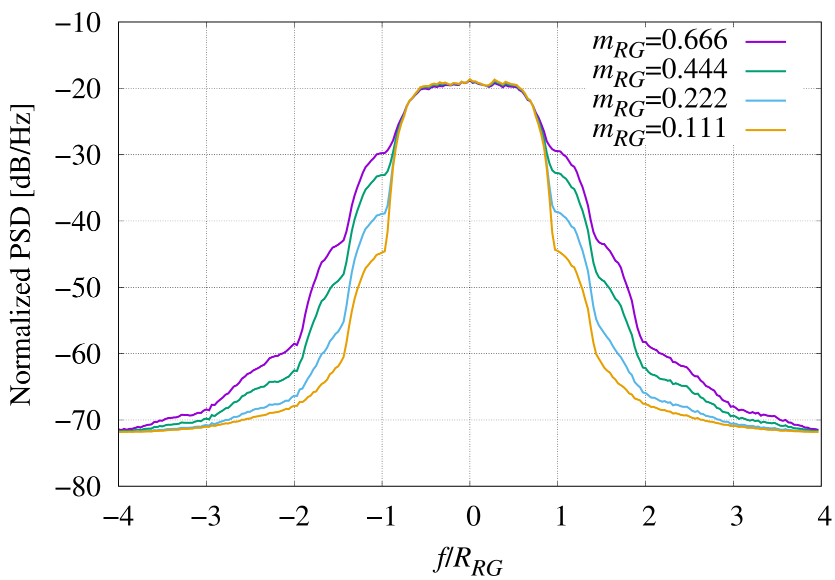

Figure 4.6: Power spectral density of 8-PSK (SRRC with roll-off 0.35) for T4B PN code under AWGN.

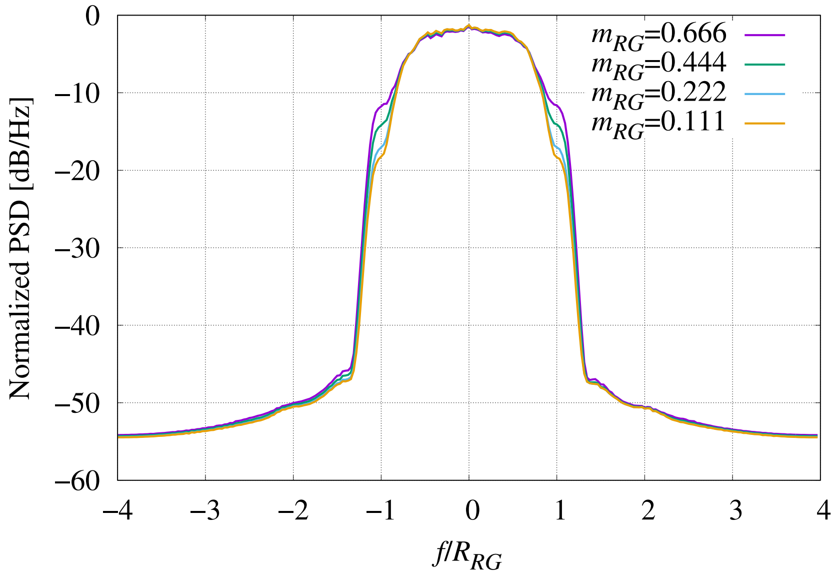

Figure 4.7: Power spectral density of QPSK (SRRC with roll-off 0.35) with TWTA for T4B PN code.

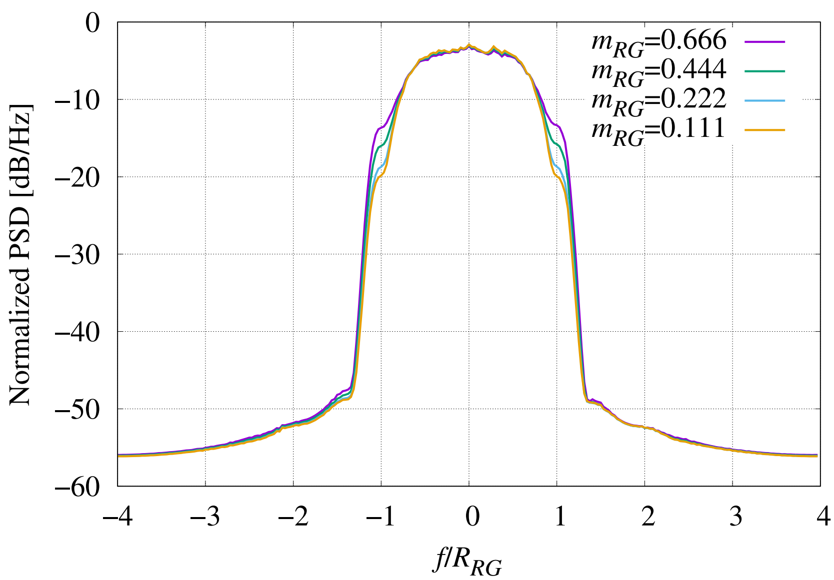

Figure 4.8: Power spectral density of 8-PSK (SRRC with roll-off 0.35) with TWTA for T4B PN code.

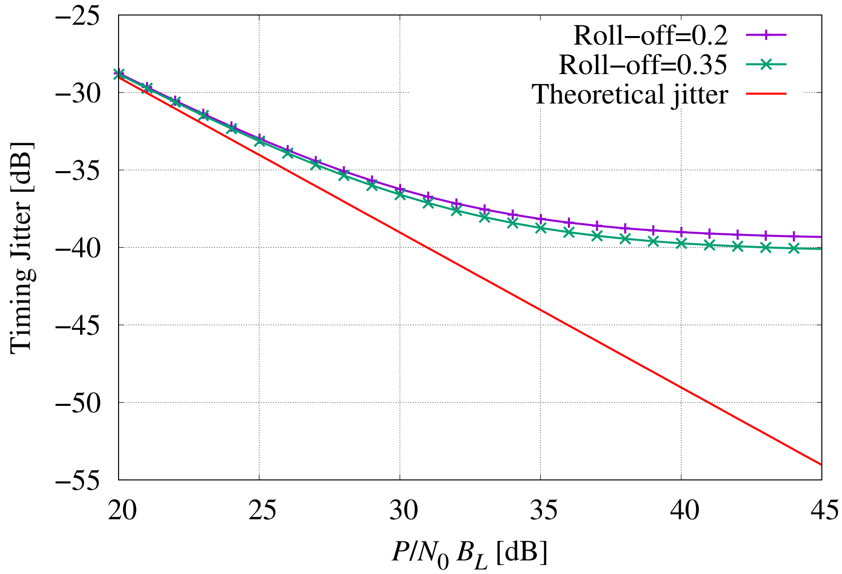

Figure 4.9: Timing jitter $\widetilde{\sigma}_\tau^2$ of QPSK-PN Ranging system under ideal telemetry cancellation condition compared to the theoretical curve.

4.1.2 Receiver Ranging Performance

The receiver performance of the ranging coupled with PSK-modulated telemetry signals has been analyzed according to an open-loop, adopting the equivalent scheme of Fig. 3.25. However, the GMSK telemetry transmitter has been replaced with an SCCC modulator followed by SRRC filter. In this respect, the normalized timing jitter for the telemetry signal reveals a significant deviation from the theoretical curve of Eq. (2.11), as is clear from Fig. 4.9. The latter has been obtained by tuning the CTL with $\gamma = 10^{-2}$ ($B_L = 15$ kHz), and it reports measurements using two different roll-off factors: 0.22 and 0.35. Besides a slight improvement of the jitter for a roll-off factor of 0.35, the two curves exhibit a noise floor as $P/N_0 B_L$ grows. To find the origin of such behavior, the problem has been studied in depth. At first, a square window (instead of the standard SRRC) has been used to filter the constellation points. In this way, the telemetry signal benefits from the constant envelope property and, as shown in Fig. 4.10, the trend equals that of GMSK-PN Ranging system: a perfect matching to the theoretical curve.

Having established that the increased timing jitter's noise floor results from the amplitude of the telemetry signal, the second RHS term in (4.6) has been probed. Below follows the mathematical proof that the noise $w^{'}(t)$ in (4.6) is not colored by the multiplication for the complex conjugate of the telemetry signal.

Proof Let us consider $w^{'}(t) = w(t)\, x_{TM}^*(t)$, recalling that $w(t) \sim \mathcal{N}(0, \sigma_N^2)$ with $\sigma_N^2 = N_0$. In the discrete time domain we have $w_n^{'} = w_n x_n^*$.

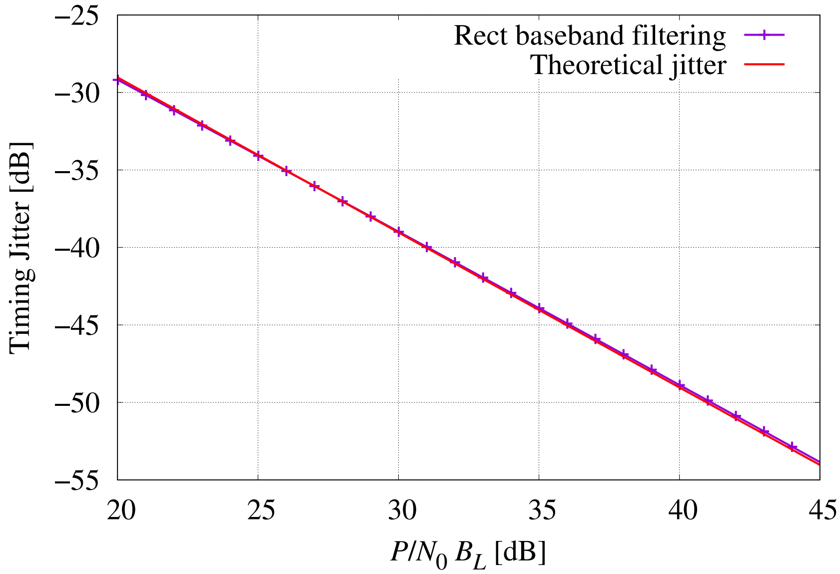

Figure 4.10: Timing jitter $\widetilde{\sigma}_\tau^2$ of QPSK(Rect filtered)-PN Ranging system under ideal telemetry cancellation condition compared to the theoretical curve.

The autocorrelation $R_{w'}$ of $w_n^{'}$ can be computed as

$$\begin{aligned} R_{w'} &\triangleq \mathbb{E}[w_n^{*'} w_{n-k}^{'}] && (4.7)\\ &= \mathbb{E}[(w_n^* x_n)(w_{n-k} x_{n-k}^*)] && (4.8)\\ &= \mathbb{E}[w_n^* w_{n-k} x_n x_{n-k}^*]\,. && (4.9) \end{aligned}$$

Because of the independence of w_n and x_n, it holds that

$$\begin{aligned} R_{w'} &= \mathbb{E}[w_n^* w_{n-k}]\mathbb{E}[x_n x_{n-k}^*] && (4.10)\\ &= \begin{cases} 0 & k \neq 0 \\ \mathbb{E}[|w_n|^2]\mathbb{E}[|x_n^*|^2] = \sigma_N^2 \sigma_x^2 & k = 0 \end{cases} && (4.11)\\ &= \sigma_N^2 \sigma_x^2 \delta_{nk} && (4.12) \end{aligned}$$

where $\sigma_x^2 = \mathbb{E}[|x_{TM}(t)|^2] = 1$ is the telemetry signal variance and δ_{nk} is the Kronecker delta. The autocorrelation function is a Dirac delta, therefore $w^{'}(t)$ is a white process with variance N_0. ■

In conclusion, the origin of the timing jitter's noise floor has been identified to be the first RHS term in (4.6). To further investigate the problem, the CTL has been analyzed. Since it has been proved that the second RHS term is still white noise, and knowing that $\mathbb{E}[|x_{TM}(t)|^2] = 1$, Eq. (4.6) can be re-written as

$$
\begin{aligned}
y(t)x^*_{TM}(t) &= r_{RG}(t) \cdot (p(t) + 1) + w'(t) && (4.13)\\
&= r_{RG}(t) + w'(t) + r_{RG}(t) \cdot p(t) && (4.14)
\end{aligned}
$$

where $p(t) = |x_{TM}(t)|^2 - 1$ is the telemetry signal power having mean value 0. Recalling that the CTL extracts the imaginary part of its input signal, for each of the three components of Eq. (4.14) (the last two of which represent an interfering term), the variance of the corresponding mid-phase integrator output has been computed to inspect the final timing jitter σ^2_τ. Without loss of generality, the following proof is provided for $m_{RG} = \frac{\pi}{2}$ and square-shaped chips, for which $r_{RG}(t) = \Phi_{RG}(t)$. However, the proof can be easily extended to any modulation index and to sine-shaped chips.

1. $\boldsymbol{r_{RG}(t)}$
   Recalling that at each clock, the mid-phase integrator computes the integral between two adjacent chips, as in Fig. 2.6, when $r_{RG}(t)$ is input to the CTL, the output is

$$
\int_{-\frac{T_c}{2}+\varepsilon}^{0} \sqrt{P}\,\mathrm{d}t - \int_{0}^{\frac{T_c}{2}+\varepsilon} \sqrt{P}\,\mathrm{d}t = -2\sqrt{P}\varepsilon\,, \tag{4.15}
$$

   thus, with zero variance, this term does not impact on σ^2_τ.

2. $\boldsymbol{w'(t)}$
   Without loss of generality, it is possible to compute the integral over the chip duration in $[0, T_c]$ as

$$
n = \int_0^{T_c} w'(t)\mathrm{d}t. \tag{4.16}
$$

   Note that, since $w^{'}(t)$'s imaginary component is still a white process with power spectral density N_0, with an abuse of notation, it is referred to as $w^{'}(t)$. Then, applying the sampling theorem to $w^{'}(t)$

$$
n = \sum_{k=0}^{n_s-1} w^{'}_k T_s \tag{4.17}
$$

   where $w'_k \sim \mathcal{N}(0, \frac{N_0}{T_s})$ is the k-th noise sample obtained by sampling $w^{'}(t)$ at sampling time kT_s, being $T_s = \frac{T_c}{n_s}$ and n_s the oversampling factor. Thus,

$$
\sigma^2_n = \mathbb{E}[|n|^2] = n_s\,\mathbb{E}\left[\left|w'_k \frac{T_c}{n_s}\right|^2\right] = T_c N_0\,. \tag{4.18}
$$

3. $\boldsymbol{r_{RG}(t) \cdot p(t)}$
   Defining $\zeta \triangleq \int_0^{T_c} r_{RG}(t) \cdot p(t)\mathrm{d}t$, as the output of the mid-phase integrator giving $r_{RG}(t) \cdot p(t)$ input to CTL, its variance is

$$
\mathbb{E}[|\zeta|^2] = \int_0^{T_c}\int_0^{T_c} \mathbb{E}[r_{RG}(t_1) \cdot r_{RG}(t_2) \cdot p(t_1) \cdot p(t_2)]\,\mathrm{d}t_1\mathrm{d}t_2. \tag{4.19}
$$

It is well-established that the autocorrelation of a wide-sense stationary process has its maximum value in 0, therefore, because of the independence of $p(t)$ and $r_{RG}(t)$, it holds

$$\mathbb{E}[|\zeta|^2] \leq \int_0^{T_c} \int_0^{T_c} \mathbb{E}[|r_{RG}(t)|^2 \cdot p^2(t)] \mathrm{d}t_1 \mathrm{d}t_2 = P\sigma_P^2 T_c^2, \tag{4.20}$$

with $\sigma_P^2 = \mathbb{E}[|p(t)|^2]$ and $P = \mathbb{E}[|\Phi_{RG}(t)|^2]$ [1], i.e the useful power of the ranging signal.

As shown in [7], and referring to it for a better understanding of the next calculations, using the linearized model of the CTL (Fig. 2.7), the loop timing jitter can be derived. Defining the loop error η at the k-th time as

$$\eta_k = \varepsilon_k + \frac{n_k}{K_\varepsilon}, \tag{4.21}$$

input to the Loop filter with transfer function $H(f)$, it holds

$$p_\tau(f) = \left| \frac{H(f)}{1 + H(f)} \right|^2 p_\eta(f), \tag{4.22}$$

where, $p_\eta(f)$ and $p_\tau(f)$ are the input and output power spectral density, respectively. Integrating (4.22) in $[0, 1/T_c]$, the jitter variance σ_τ^2 is given by

$$\sigma_\tau^2 = T_c \int_0^{1/T_c} p_\tau(f) \mathrm{d}f = T_c \int_0^{1/T_c} \left| \frac{H(f)}{1 + H(f)} \right|^2 \cdot p_\eta(f) \mathrm{d}f. \tag{4.23}$$

Thus, if η is a white process, then $p_\eta(f) = \sigma_\eta^2$ and the loop timing jitter becomes

$$\sigma_\tau^2 = B_L T_c \cdot \sigma_\eta^2. \tag{4.24}$$

Specifically, for the second RHS term in (4.14), $\sigma_\eta^2 = \frac{N_0 T_c}{4P}$, resulting in the timing jitter of (2.11) (for the square pulse shape).
Whereas, for the third RHS term in (4.14), $\sigma_\eta^2 = \frac{P\sigma_P^2 T_c^2}{4P}$, leading to an additional jitter equals to

$$\frac{(\sigma_P^2 B_L T_c)}{4} T_c^2. \tag{4.25}$$

Moreover, to apply Eq. (4.24), it has been assumed $|x_{TM}(t)|^2$ to be white, a fairly good assumption since two adjacent integrated symbols of the telemetry signal power over two different symbols times are almost uncorrelated. In support of the claim, Fig. 4.11 presents the normalized autocorrelation for a QPSK-modulated telemetry signal power.

The ranging jitter in (4.25) is due to the fact that $|x_{TM}(t)|^2 \neq 1$. In conclusion, the overall timing variance, in presence of non-constant envelope modulations, is upper bounded by

$$\sigma_\tau^2 \leq \frac{B_L}{4(P/N_0)} T_c^2 + \frac{(\sigma_P^2 B_L T_c)}{4} T_c^2. \tag{4.26}$$

Note that the above calculations are applicable to both PSK and APSK modulation formats.

[1] Note that for the case of study $\mathbb{E}[|r_{RG}(t)|^2] = \mathbb{E}[|\Phi_{RG}(t)|^2]$.

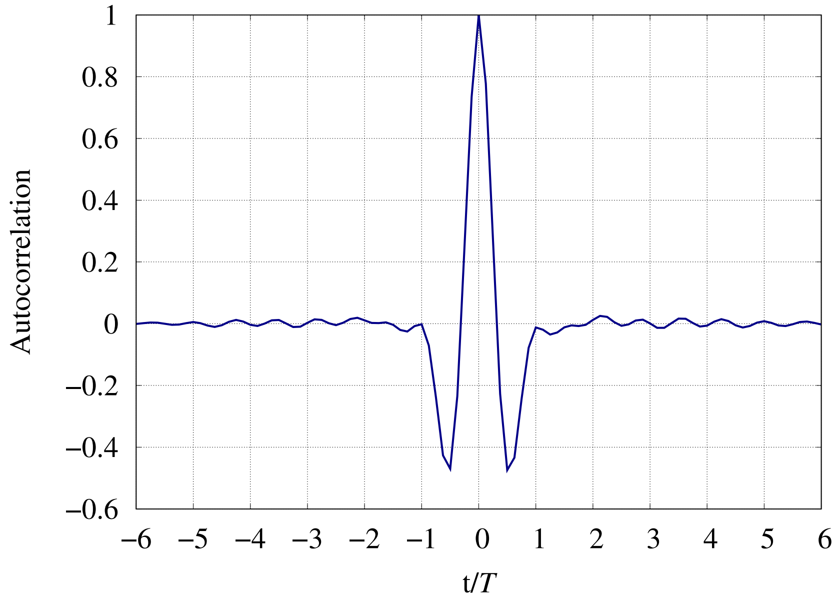

Figure 4.11: Normalized autocorrelation for QPSK telemetry signal power $|x_{TM}(t)|^2$.

Roll-off	QPSK	8-PSK
0.2	0.240	0.243
0.25	0.224	0.226
0.3	0.209	0.211
0.35	0.197	0.199

Table 4.4: Power jitter σ_P^2 for PSK modulations.

The variance of $p(t)$, σ_P^2, was measured for QPSK and 8-PSK modulations and for different roll-off factors. The results are reported in Tab. 4.4. It can be observed that, as long as the P/N_0 is small, the first RHS term in (4.26) dominates over the second. For this reason, the simulated normalized ranging jitter in Fig. 4.9 is close to the theoretical one for low values of P/N_0B_L, while deviating from it as P/N_0B_L grows. As evidenced by (4.26), the supplementary timing jitter in (4.25) is directly proportional to the loop bandwidth B_L. Thus, by reducing B_L, it can be lowered as Fig. 4.12 and 4.13 attest. In them, the loop bandwidth considered were 15 kHz ($\gamma = 10^{-2}$), 1.5 kHz ($\gamma = 10^{-3}$) and 150 Hz ($\gamma = 10^{-4}$).

The performance analysis of the CTL for the QPSK/8-PSK-PN Ranging system has also been extended to the case of non-ideal telemetry cancellation. For this purpose, the detection of the telemetry stream has been simulated in accordance with the theoretical modulation BER in a genie-aided scheme similar to that of Fig. 3.25. Additionally, extra noise levels were introduced to account for potential channel impairments.

The BER for the QPSK modulation is the same expressed in (3.17). The BER for the 8-PSK

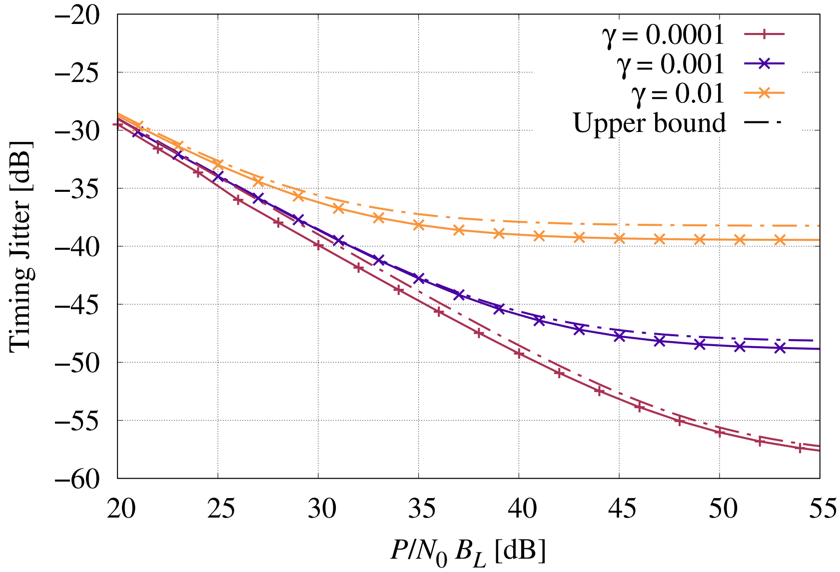

Figure 4.12: Timing jitter $\widetilde{\sigma}_\tau^2$ for QPSK-PN Ranging system.

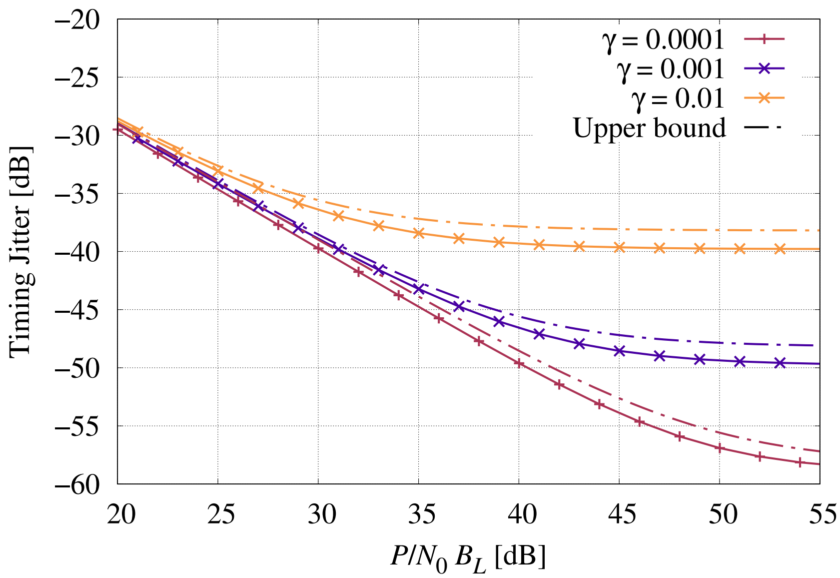

Figure 4.13: Timing jitter $\widetilde{\sigma}_\tau^2$ for 8-PSK-PN Ranging system.

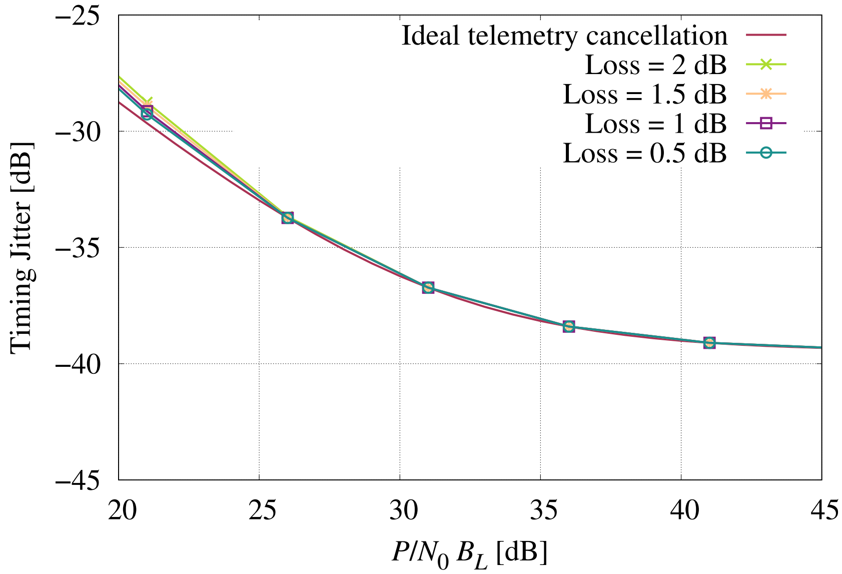

Figure 4.14: Timing jitter $\widetilde{\sigma}_\tau^2$ for ideal and noisy QPSK telemetry cancellation, $B_L = 15$ kHz.

modulation has been derived using the closed formula [24]

$$P_b = \frac{1}{3}\text{erfc}\left(\sqrt{\log_2 8 \cdot \sin^2\left(\frac{\pi}{8}\right) \cdot \frac{E_b}{N_0}}\right), \tag{4.27}$$

which constitutes a good approximation only for large values of E_b/N_0. For low values of E_b/N_0, instead, the BER has been limited to 0.5.

Fig. 4.14, 4.15, and 4.16 show how the noisy telemetry cancellation with QPSK impacts on the ranging as already observed for the GMSK-PN Ranging system (Fig. 3.27). For what concerns 8-PSK, despite the higher impact of the cancellation noise on the jitter due to the higher modulation order and regardless of the noise level added to the nominal BER, all the curves (Fig. 4.17, 4.18, and 4.19) asymptotically match the ideal one. Even though in this case the convergence occurs later than in the GMSK and QPSK cases, the gap from the theoretical curve is about 1 dB.

4.2 APSK and PN Ranging

This section will focus on the combination of the PN Ranging with APSK modulations. In particular, among the different ACM formats in the standard, the discussion will be limited to 13, 18 and 23 ACM.

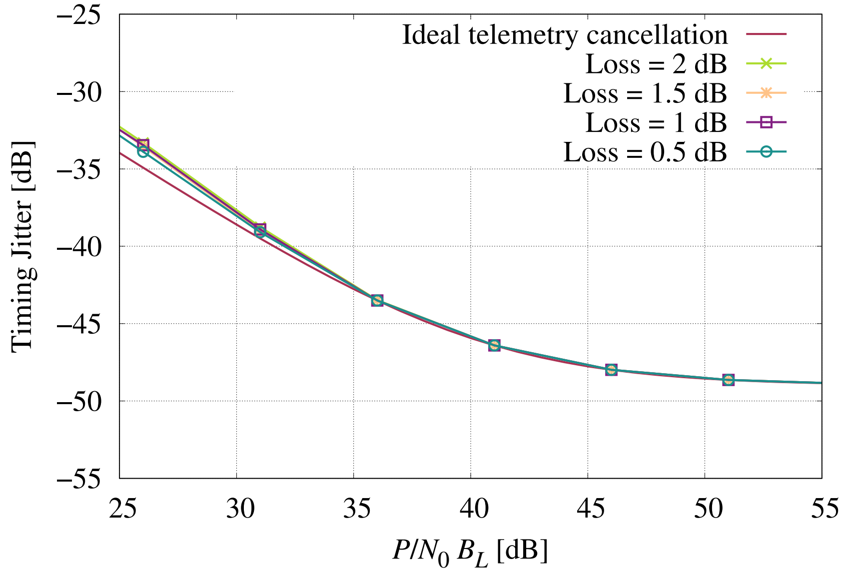

Figure 4.15: Timing jitter $\widetilde{\sigma}_\tau^2$ for ideal and noisy QPSK telemetry cancellation, $B_L = 1.5$ kHz.

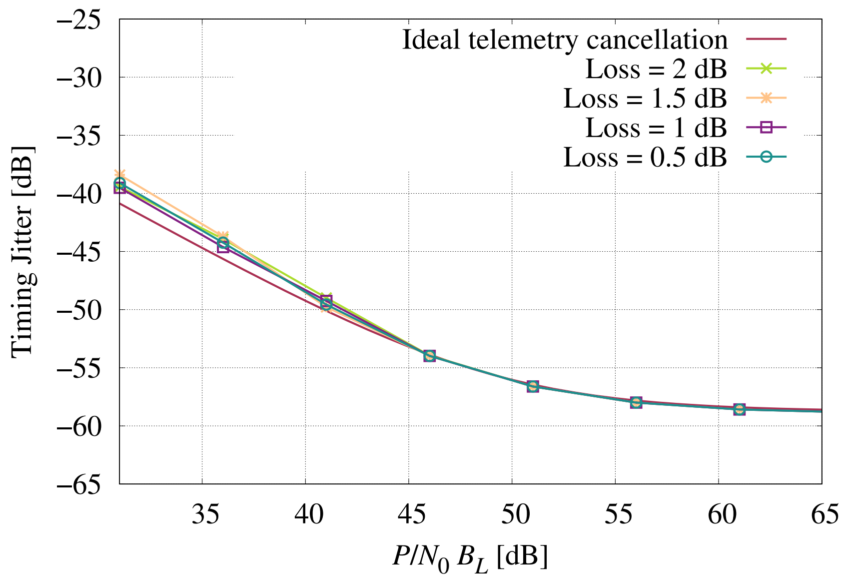

Figure 4.16: Timing jitter $\widetilde{\sigma}_\tau^2$ for ideal and noisy QPSK telemetry cancellation, $B_L = 150$ Hz.

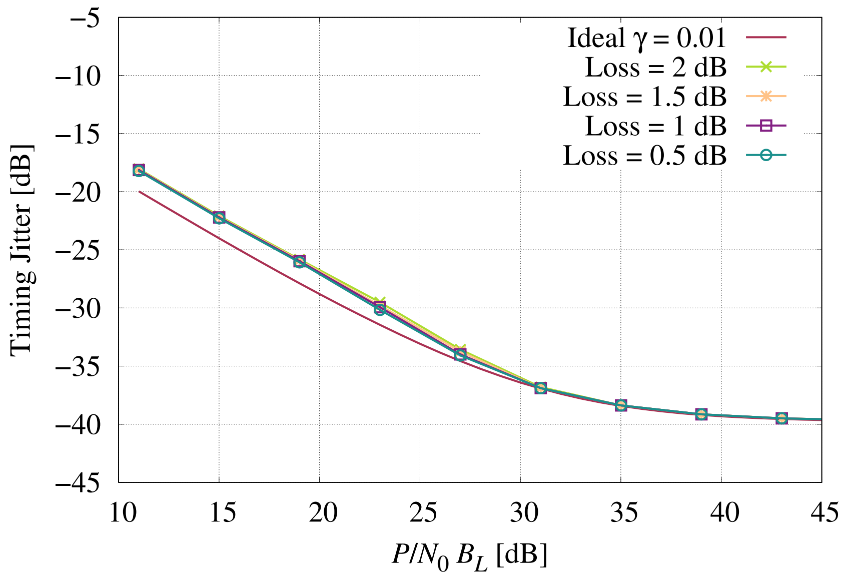

Figure 4.17: Timing jitter $\widetilde{\sigma}_\tau^2$ for ideal and noisy 8-PSK telemetry cancellation, $B_L = 15$ kHz.

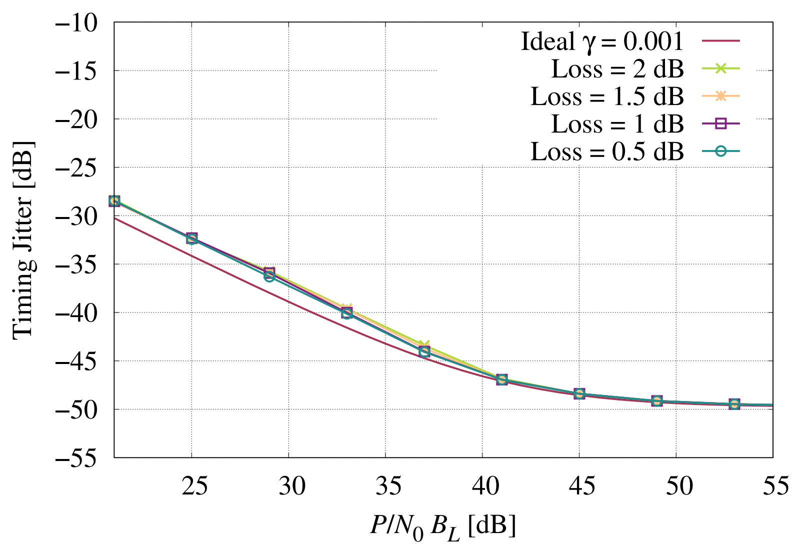

Figure 4.18: Timing jitter $\widetilde{\sigma}_\tau^2$ for ideal and noisy 8-PSK telemetry cancellation, $B_L = 1.5$ kHz.

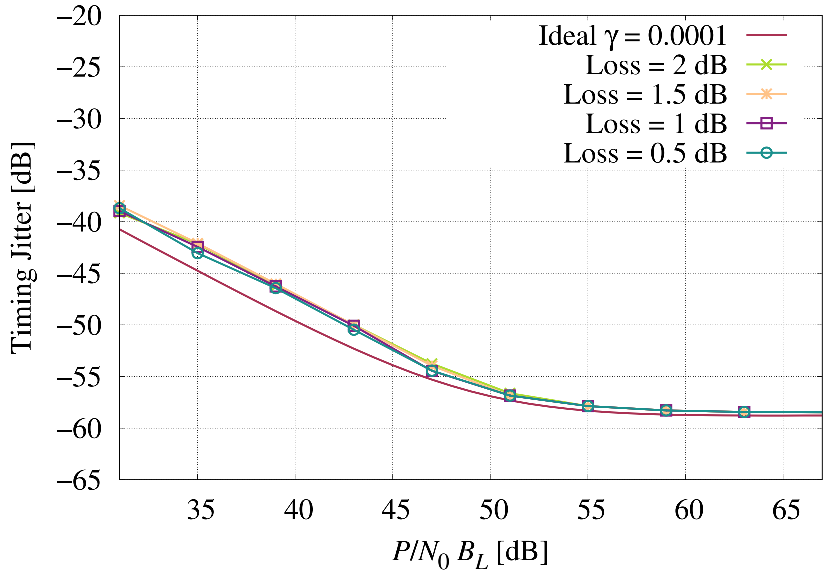

Figure 4.19: Timing jitter $\widetilde{\sigma}_{\tau}^{2}$ for ideal and noisy 8-PSK telemetry cancellation, $B_L = 150$ Hz.

ACM format	OBO [dB]	IBO [dB]
13	1.74	1.5
18	3.45	3
23	4.2	3.5

Table 4.5: Optimal OBO and corresponding IBO for 13, 18 and 23 ACM.

4.2.1 Spectral Occupancy

Likewise, for APSK modulations, the 99-percent bandwidth of 16-APSK, 32-APSK and, 64-APSK was measured under AWGN. As expected, it matched those of PSK modulations showed in Tab. 4.2.

For the non-linear case, the IBO corresponding to the optimal OBO that minimizes the total degradation was chosen for each ACM. These values are provided in Tab. 4.5 while the associated 99-percent bandwidth (normalized to R_{TM}) measures in Tab. 4.6. The last emphasizes the spectral efficiency of the newly introduced modulation schemes, already proved by the PSK bandwidth results. As for the PSK modulations, a telemetry channel symbol rate and a chip rate of 4.2 Msymbol/s and 3 Mchip/s, respectively, have been considered in simulation.

4.2.2 Ranging Performance

As previously outlined, the mathematical derivation (4.1.2), which led to the definition of the upper-bound for the ranging jitter, also applies to the APSK modulations. For them, the power

m_{RG}	13 ACM		18 ACM		23 ACM	
	T2B	T4B	T2B	T4B	T2B	T4B
0.111	1.21	1.23	1.19	1.21	1.16	1.16
0.222	1.23	1.25	1.21	1.21	1.21	1.21
0.444	1.34	1.43	1.34	1.38	1.29	1.39
0.666	1.47	1.47	1.47	1.47	1.47	1.47

Table 4.6: TWTA 99% bandwidth for APSK-modulated telemetry (SRRC with roll-off 0.35).

Roll-off	16APSK	32APSK	64APSK
0.2	0.435	0.560	0.483
0.25	0.426	0.554	0.474
0.3	0.418	0.551	0.467
0.35	0.412	0.549	0.462

Table 4.7: Power jitter σ_P^2 for APSK modulations.

jitter σ_p^2 has been computed and reported in Tab. 4.7. The higher peak-to-average power ratio of 32-APSK, greater than that of 16-APSK and 64-APSK [5], explains the larger σ_p^2 of the former.

Fig. 4.20, 4.21, and 4.22 present the normalized timing jitter for 16-APSK, 32-APSK and 64-APSK modulations, respectively. From these figures, it is clear that the timing variance exhibits the same trend that characterized the PSK modulations. For a better comparison, Fig. 4.23 reports the normalized timing jitter for the three modulation formats, simulated under the ideal telemetry cancellation assumption and adopting $B_L = 1.5$ kHz. This last figure highlights how $\widetilde{\sigma}_\tau^2$ for 64-APSK gains with respect to the other two, whereas the 32-APSK has the highest jitter among the three. The inferior performance of the latter is justified by its highest peak-to-average-power ratio (compared to the other two formats) and, consequently, higher power variance. Whereas, as σ_P^2 is almost the same for 16-APSK and 64-APSK, it is believed that the reason for the better performance of the last modulation scheme lies in the correlation function of Eq. (4.19). In fact, it has a narrower peak within the symbol time as the constellation grows, due to the less correlation between one channel symbol and the next, resulting in a smaller integral. Moreover, it can be observed that because of the lower timing jitter, the upper-bound computed for the 64-APSK modulation gets looser.

Also, for the APSK set of modulations, the receiver's performances have been tested in noisy conditions. Because of the lack of a closed formula, the BER curves have been simulated for uncoded ACM formats (see Fig. 4.24). Then, the required BER has been obtained by applying a linear fitting to the simulated curve and then using it to simulate the telemetry symbols' reception.

In this section, the CTL performance is reported for 16-APSK modulation with $B_L = 15$ kHz (see Fig 4.25). As already proved by the previous results, the curves exhibit the same trend despite the impact of the noise, being the last dependent on the cardinality of the modulation scheme.

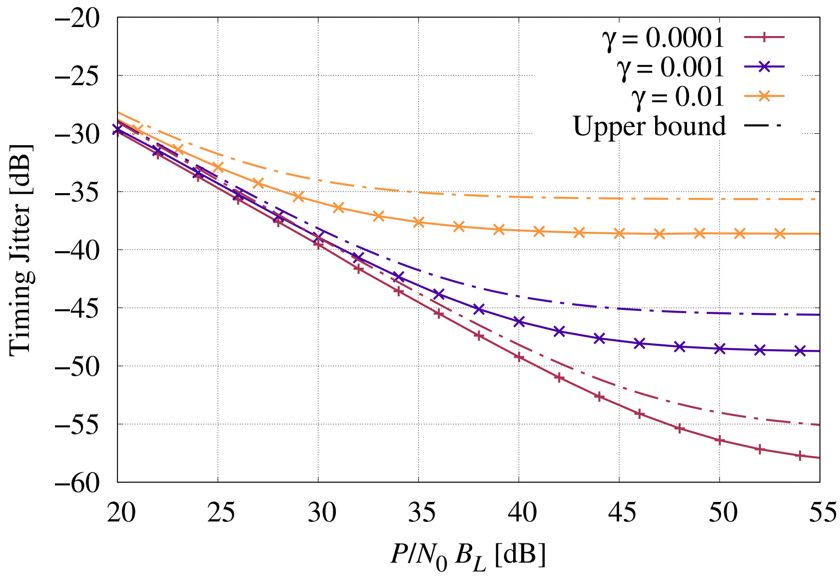

Figure 4.20: Timing jitter $\widetilde{\sigma}_\tau^2$ for 16-APSK-PN Ranging system.

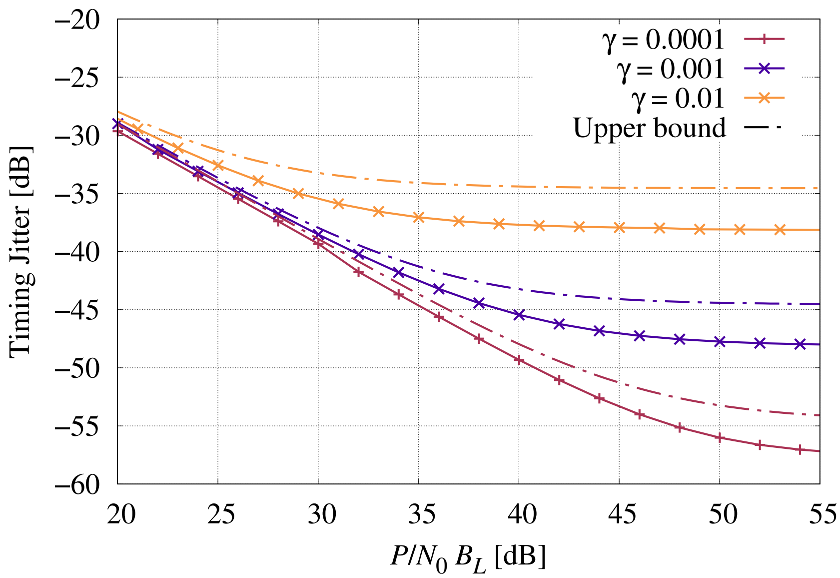

Figure 4.21: Timing jitter $\widetilde{\sigma}_\tau^2$ for 32-APSK-PN Ranging system.

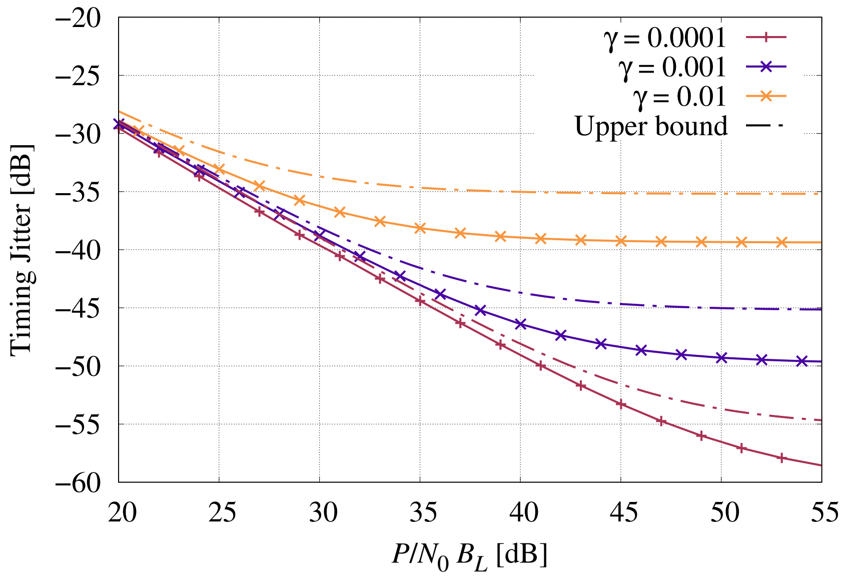

Figure 4.22: Timing jitter $\widetilde{\sigma}_\tau^2$ for 64-APSK-PN Ranging system.

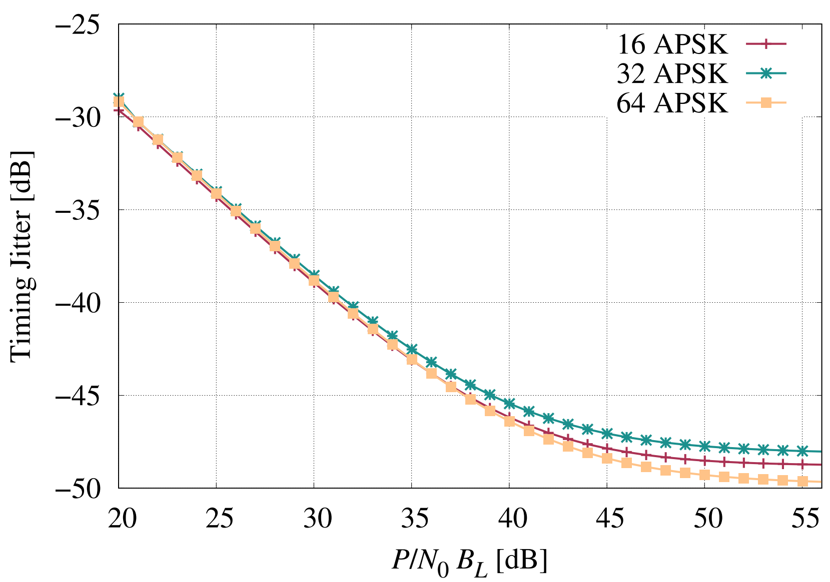

Figure 4.23: Timing jitter $\widetilde{\sigma}_\tau^2$ comparison under ideal condition for APSK constellations.

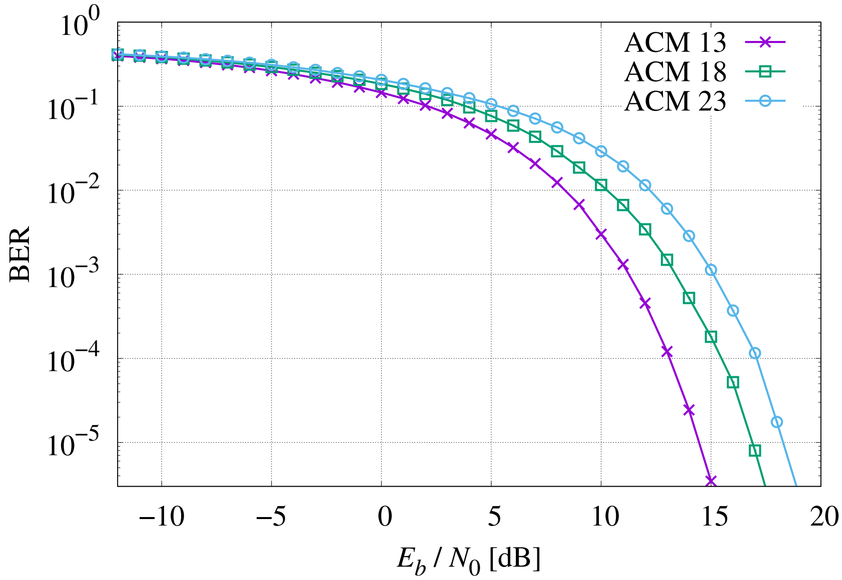

Figure 4.24: BER for uncoded APSK constellations

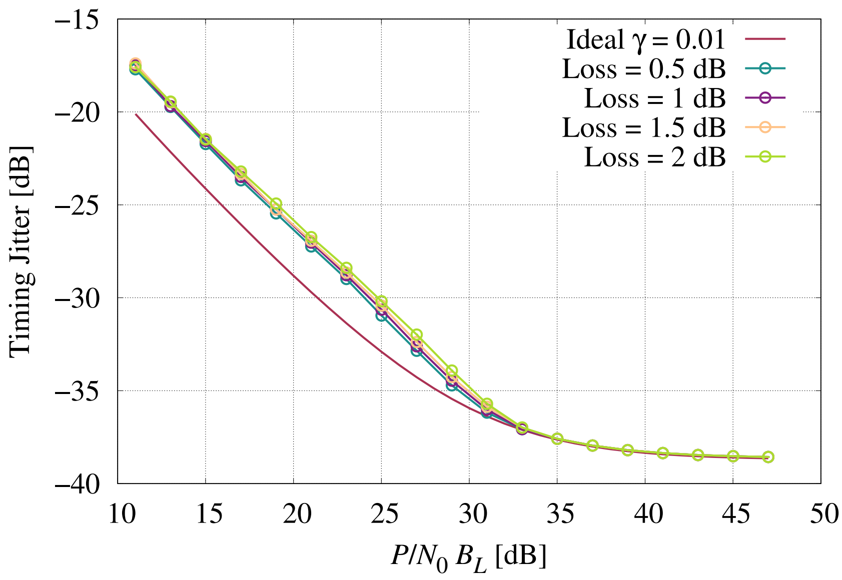

Figure 4.25: Timing jitter $\tilde{\sigma}_\tau^2$ for ideal and noisy 16-APSK telemetry cancellation, $B_L = 15$ kHz

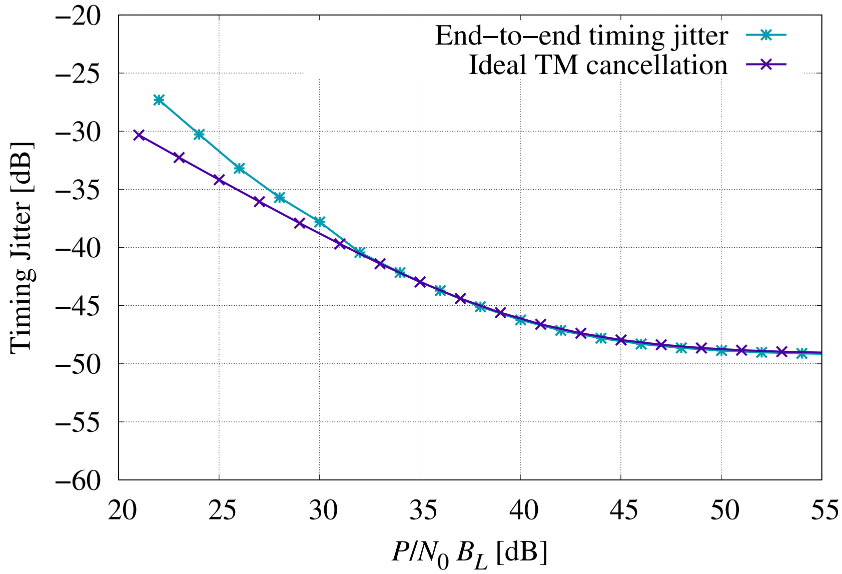

Figure 4.26: End-to-end timing jitter $\widetilde{\sigma}_\tau^2$ versus ideal one for QPSK telemetry and $B_L = 1.5$ kHz.

4.3 End-to-end Numerical Results

The details of the closed-loop receiver used to implement the SCCC-PN Ranging system have been already disclosed as an introduction to this chapter. Hence, in this section, the findings coming from the full TX-RX chain simulations are presented. For what concerns the timing jitter, by looking at Fig. 4.26 and 4.27, it can be seen how the PSK modulations generally maintain the same trend already revealed by the open-loop scenario. In fact, besides an increase, for low values of P/N_0B_L, of the gap between the simulated and the ideal curve, where, for the last, no cancellation noise has been introduced, the two curves end up coinciding as P/N_0B_L grows. As expected and as already proved by the open-loop results, the 8-PSK shows a greater discrepancy with respect to the ideal case than QPSK. Despite the reciprocity between telemetry and ranging performance, the jitter discrepancy with respect to the ideal case for low values of P/N_0B_L is not reflected in a mismatch of the end-to-end simulated BER and the theoretical one, as evidenced by Fig. 4.28.

Similar observations can be made for the APSK modulation set. In general, as the modulation order increases the matching of the ideal and the simulated curve shifts to higher values of P/N_0B_L. However, similar results were obtained from the open-loop analysis. As already highlighted for the PSK modulations, the end-to-end BER for the three modulations does not differ from the theoretical ones, as can be seen in Fig 4.32.

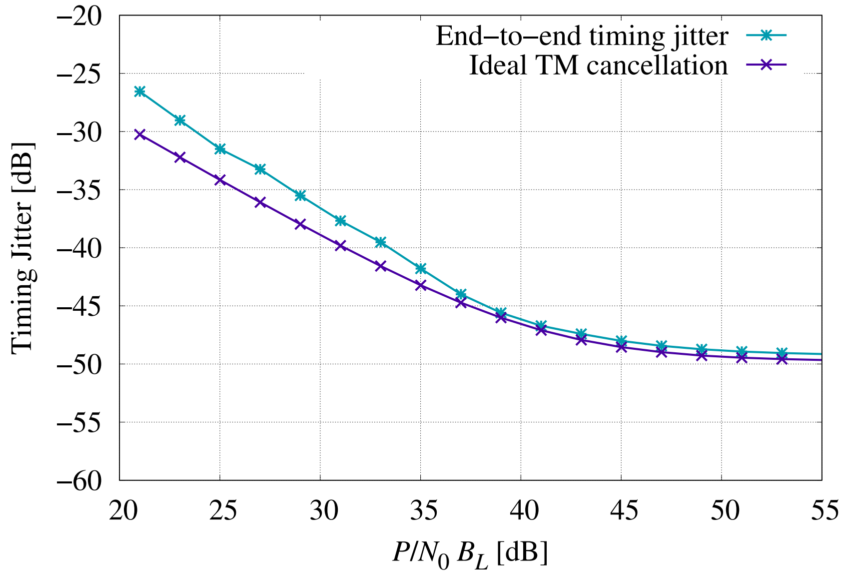

Figure 4.27: End-to-end timing jitter $\widetilde{\sigma}_{\tau}^{2}$ versus ideal one for 8-PSK telemetry and $B_L = 1.5$ kHz.

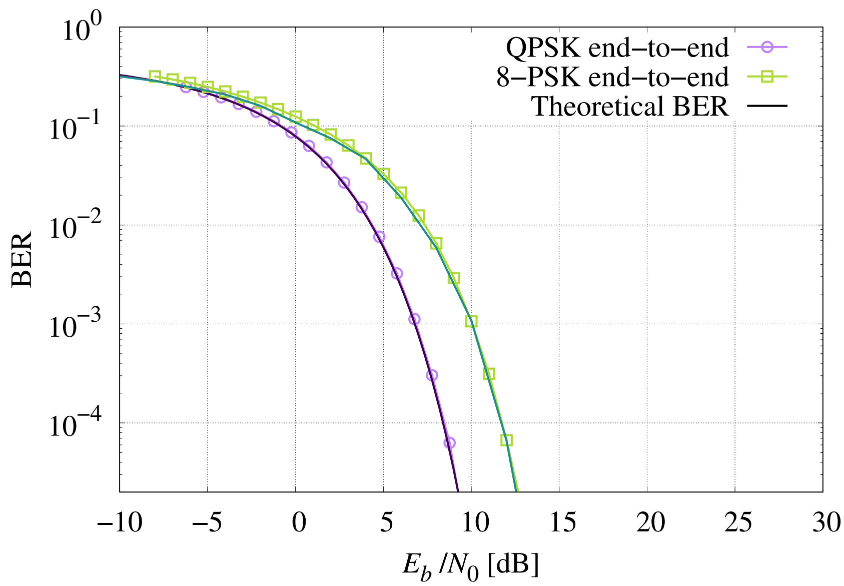

Figure 4.28: BER resulting from the ranging cancellation of a closed-loop receiver for QPSK and 8-PSK telemetry versus theoretical BER.

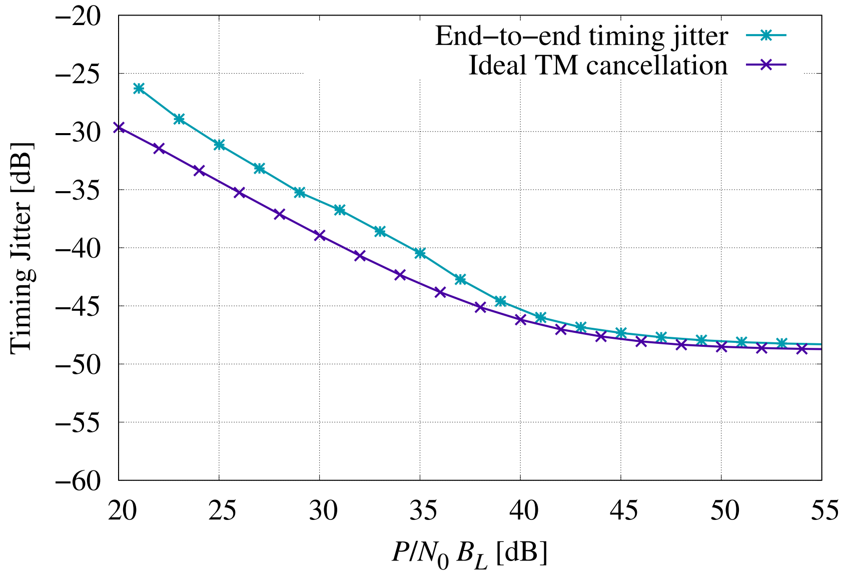

Figure 4.29: End-to-end timing jitter $\widetilde{\sigma}_\tau^2$ versus ideal one for 16-APSK telemetry and $B_L = 1.5$ kHz.

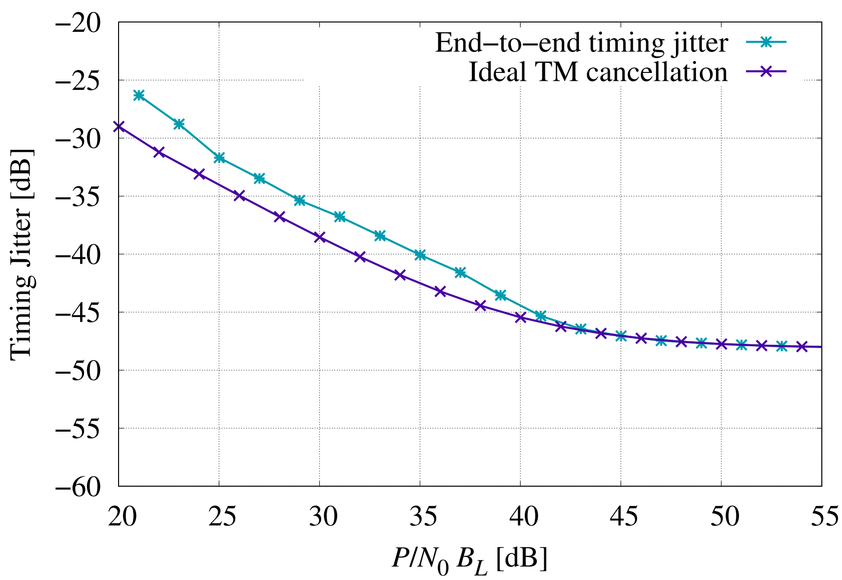

Figure 4.30: End-to-end timing jitter $\widetilde{\sigma}_\tau^2$ versus ideal one for 32-APSK telemetry and $B_L = 1.5$ kHz.

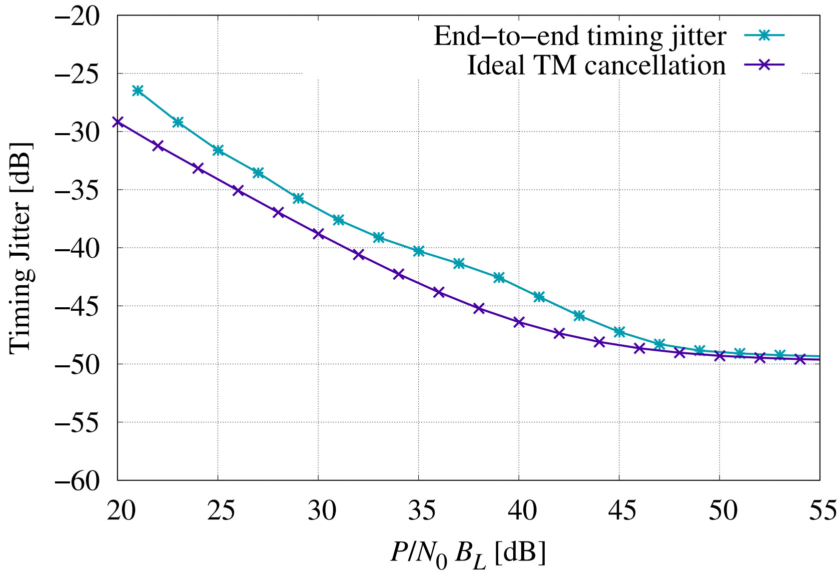

Figure 4.31: End-to-end timing jitter $\widetilde{\sigma}_{\tau}^{2}$ versus ideal one for 64-APSK telemetry and $B_L = 1.5$ kHz.

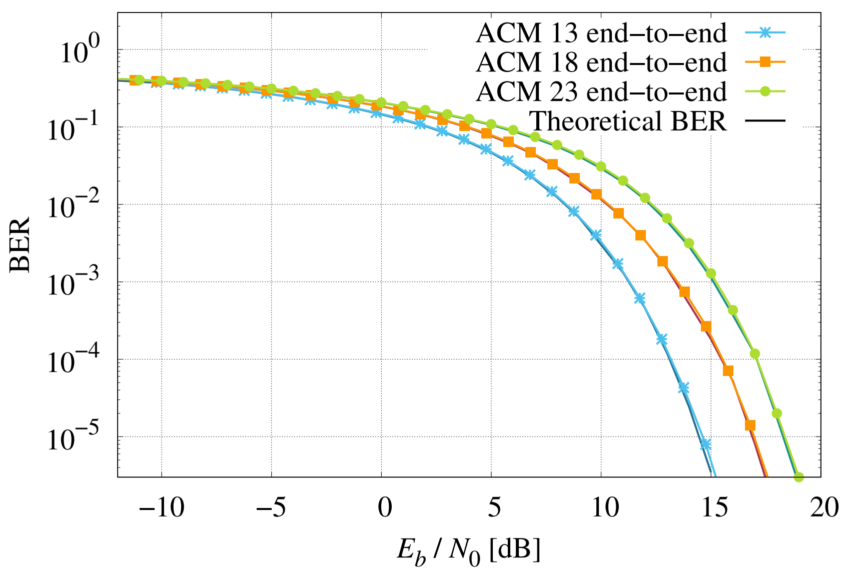

Figure 4.32: BER resulting from the ranging cancellation of a closed-loop receiver for 16-APSK, 32-APSK and 64-APSK telemetry versus theoretical BER.

Chapter 5

System Analysis of Lagrange Missions

This chapter analyzes the advantages of implementing the SCCC-PN Ranging system in a classical Science mission orbiting around the second Lagrange point (L2) of the Sun-Earth system [25]. For this study, two examples will be considered: the GAIA [11] and the future GAIA-NIR [3] missions. By using these two missions as a reference, the performance of the SCCC-PN Ranging system versus a classical GMSK-PN Ranging scheme will be provided and compared.

The remainder of this chapter is organized as follows: Section 5.1 provides the basics of the link budget, Section 5.2 presents an overview of GAIA and GAIA-NIR missions and, finally, Section 5.3 performs a detailed analysis of the classical and the innovative communication systems.

5.1 Link Budget

As well-known, the link budget accounts for the power received at the receiving equipment of a communication link. In this study, a simplified version of the standard link budget in [26] has been realized. In fact, instead of considering the variability of the involved parameters as a probabilistic function, only two cases (the best and the worst) have been accounted for. The key formula, to determine the ratio between the received signal power and the noise power, is:

$$\frac{P_{RX}}{N_0} = EIRP + G/T - FSPL - k - l - m \, [\mathrm{dB}] \, , \tag{5.1}$$

where, the Effective Isotropic Radiated Power (EIRP) characterizes the transmitter's performance. It is defined as the product of the signal power emitted after amplification and the gain of the transmitting antenna. On the other hand, the receiver's performance depends on G/T, the ratio of the antenna receive gain in a given direction (G), and the system noise temperature (T) [12]. Instead, the parameter k represents the Boltzmann's constant (1.379×10^{-23} J/K) and l includes several impairments the signal experiences during propagation (atmospheric, pointing, demodulation, degradation losses, etc.). Moreover, it is standard to incorporate a margin,

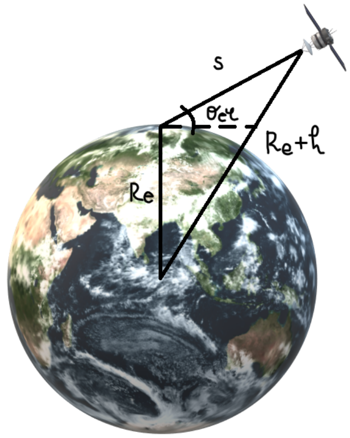

Figure 5.1: Geometrical representation of the slant range calculation.

m in (5.1), of at least 3 dB [8]. Finally, the Free Space Path Loss (FSPL) accounts for the attenuation the electromagnetic signal experiences while propagating from the transmitter to the receiver end. It is computed as

$$FSPL = 20 \cdot \log_{10}\left(\frac{4\pi s f}{c}\right) \text{ [dB]}, \tag{5.2}$$

where, c is the speed of light, f the frequency and s the slant range, that is the line of sight distance between the S/C and the G/S. The latter can be computed as function of the satellite altitude h and the elevation angle θ_{el} (i.e., the angle between the horizontal plane and the line of sight, measured in the vertical plane). In fact, by referring to Fig. 5.1, and using the cosine rule, it can be shown that

$$(R_e + h)^2 = R_e^2 + s^2 - 2R_e s \cdot \cos(90 + \theta_{el}), \tag{5.3}$$

where R_e is the Earth's radius (6378 km; assuming a perfect spherical Earth). Thus, the slant range s is the positive solution to the quadratic equation in (5.3):

$$s = \frac{2R_e \cos(90 + \theta_{el}) + \sqrt{4R_e^2 \cos^2(90 + \theta_{el}) + 4(R_e + h)^2 + R_e^2}}{2} \text{ [km]}. \tag{5.4}$$

The formulas here provided are necessary to perform the link budget analysis. Section 5.3 will rely on these equations to extract the significant quantities to the computation.

5.2 Overview of the GAIA Missions

GAIA, operational since 2014, "aims to chart a three-dimensional map of more than a thousand million stars throughout our Galaxy and beyond, mapping their motions, luminosity, temperature and composition [11]". The data obtained from this mission try to answer a wide range of

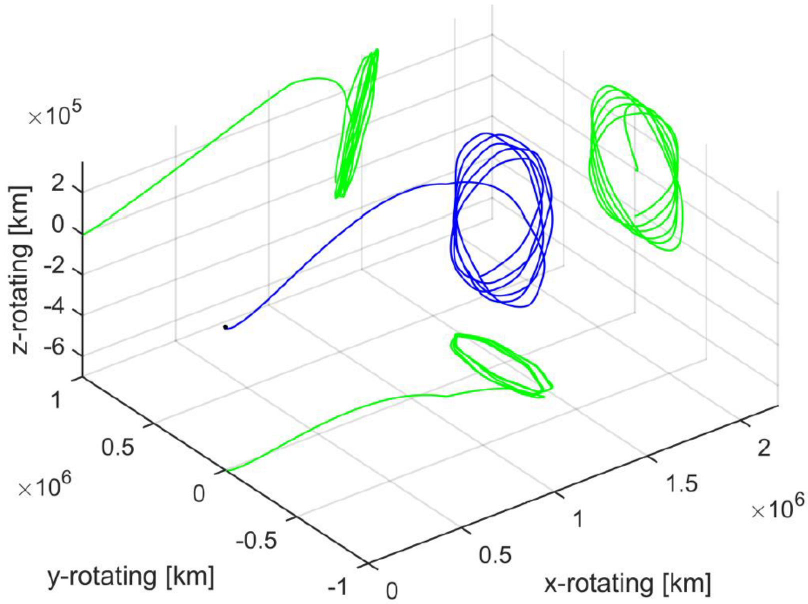

Figure 5.2: Small amplitude Lissajous orbit about the Sun-Earth libration point 2 (blue) and the projection on the axes (green) [3].

important questions related to the origin, structure, and evolutionary history of the Milky Way. To achieve its ultimate goal, GAIA operates in a Lissajous orbit around L2. In its orbit, GAIA reaches a distance of about 1.5 million km from Earth, in the anti-Sun direction. The graphical representation of the spacecraft orbit is reported in Fig. 5.2, where, the x-axis coincides with the Sun-Earth line, the z-axis is normal to the ecliptic plane, and the y-axis is oriented such that the system is a right-hand coordinate system with origin corresponding to the Earth's center [3].

Thanks to millions of celestial objects observed by GAIA over the years, the most accurate map of our Galaxy has been produced (Fig. 5.3).

GAIA-NIR, on its own, is meant to be the GAIA successor, and intending to improve the accuracy of some of the measurements taken by GAIA, and to expanding the GAIA stars' catalog with astronomical sources emitting in unexplored frequency bands (Infra-Red). Despite the maximal reuse of the technologies implemented in GAIA, to support the greater scientific objectives, GAIA-NIR's design foresees a different antenna. In fact, rather than the Phased Array Antenna (PAA) mounted on GAIA and reported in Fig. 5.4, a different PAA, which allows achieving an EIRP around 46 dB [3], has been proposed for the GAIA-NIR spacecraft (see Fig. 5.5). Such an EIRP allows the communication system to rely on higher-order modulation formats, with respect to the binary GMSK modulation supported by GAIA's transponder.

The design of the Radio Frequency Distribution Network of GAIA and GAIA-NIR is reported in Fig. 5.6. The communication system envisions two X-Band transponders for redundancy purposes, crucial to ensure safety. Each of these units is connected, by means of two different ports of a switch, to two Low Gain Antennas (LGA) and a High Gain Antenna (HGA), namely,

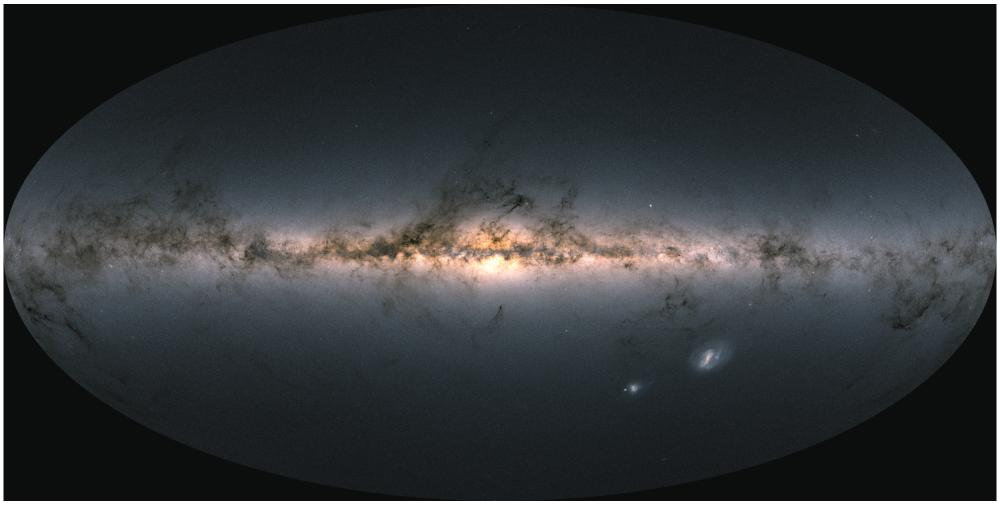

Figure 5.3: Map of the entire sky obtained using data from more than 1.8 million stars observed by ESA's GAIA satellite [4].

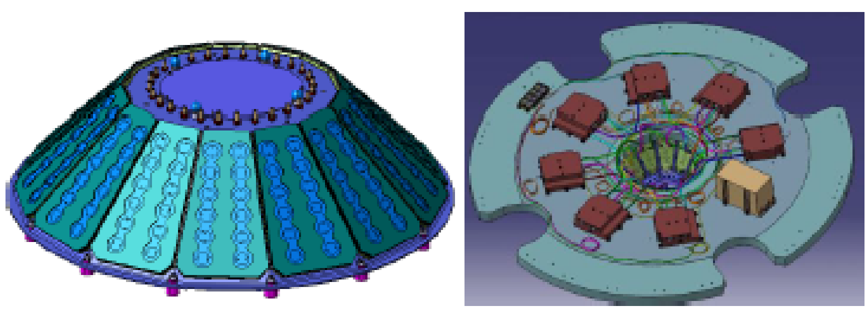

Figure 5.4: Phased Array Antenna cone (left) and RF stage (right) [3].

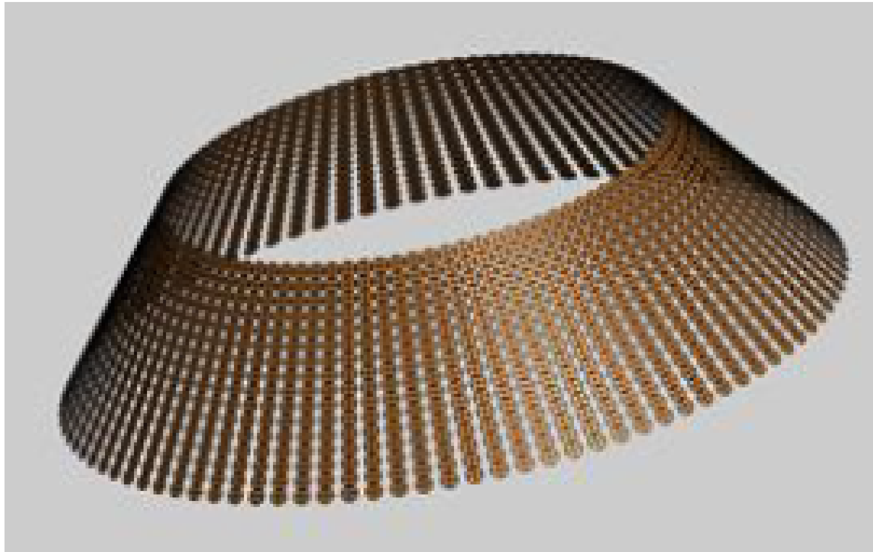

Figure 5.5: Phased Array Antenna cone (left) and low-level BFN (right) that guarantee EIRP ≥ 46.9 dB [3].

the PPA above mentioned. If the LGA is characterized by a very low gain (≈ 0 dB), the HGA is used for transmitting a high rate stream because of its greater EIRP (35 dB for GAIA, 46 dB for GAIA-NIR). A 3-dB splitter is then inserted between the transmitter and the two low gain antennas to equally divide the power between them. Of course, since the transmitter and the receiver operate at different frequencies, a diplexer is required to combine the incoming (received) and outgoing (transmitted) signals to allow the simultaneous transmission and reception of data.

5.3 Performance Comparison: SCCC versus GMSK

Tab. 5.1 reports the link budget of the GAIA and GAIA-NIR missions, based on the equations in Section 5.1. In particular, for the case of study, the Cebreros site was chosen as the receiver station. Thus, the receiver-related G/T and atmospheric losses have been set accordingly to the values provided in [27]. Moreover, the term "Demodulation Losses" in Tab. 5.1 comprises also OBO, which is different from 0 dB only for the APSK modulation formats.

When looking at the end-to-end results in Section 4.3, it can be observed from the BER curves that the demodulation loss is negligible. Hence, it can be expected that, in presence of SCCC coding, the SNR values required for achieving a CER equal to 10^{-4} will be the same as shown in Tab. 4.1 [5]. Once the P_{RX}/N_0 has been determined at the receiver, the E_b/N_0 corresponding to the required CER (10^{-4}), and that allowed to comply with the bandwidth limitation of 10 MHz [9], was selected. It turned out that GAIA's best-case scenario supports ACM 11 (8-PSK), while its worst-case scenario ACM 5 (QPSK). On the other hand, GAIA-NIR supports ACM 21 (32-APSK) at best and ACM 16 (16-APSK) at worst. A summary of the results can be found in Tab. 5.2, where the bitrate R_b has been derived as

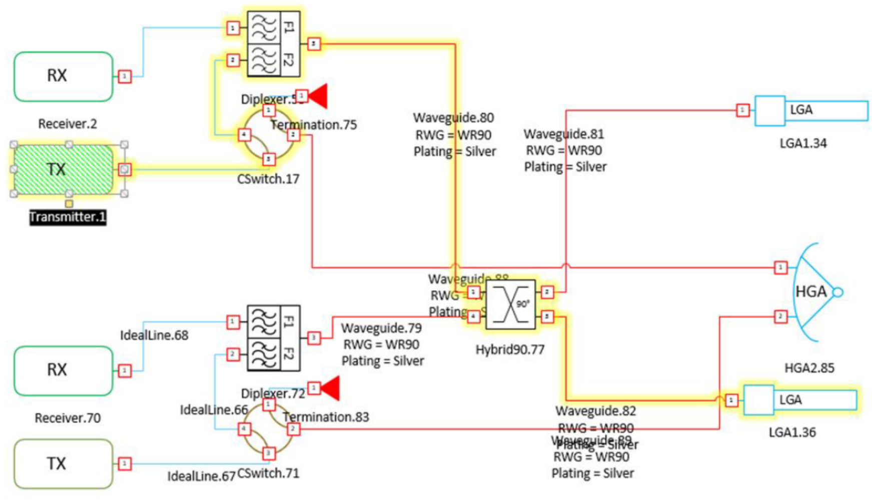

Figure 5.6: GAIA/GAIA-NIR Radio Frequency Distribution Network implementation [3].

	GAIA		GAIA-NIR	
	Best	Worst	Best	Worst
Frequency [MHz]	8500	8500	8500	8500
EIRP [dB]	34	34	45	45
S/C altitude [km]	1368000	1760000	1368000	1760000
Elevation angle [deg]	50	10	50	10
Slant Range [km]	1369486	1765259	1369486	1765259
Path Loss [dB]	234	236	234	236
Atmospheric Losses [dB]	0.27	1.04	0.27	1.04
Demodulation Losses [dB]	1.65	1	6.19	3.3
G/T [dBK]	53.1	50.2	53.1	50.2
P_{RX}/N_0 [dB]	81.7	75.8	92.7	86.8
Margin [dB]	3.3	3	3.3	3.3

Table 5.1: GAIA/GAIA-NIR link budget scenario.

	GAIA		GAIA-NIR	
	Best-case	Worst-case	Best-case	Worst-case
ACM	11	5	21	16
E_b/N_0 [dB]	5.46	2.39	8.49	6.5
R_b [Mbps]	14.5	8.9	26.5	21.1
B [MHz]	9.2	9.6	9.6	9.9

Table 5.2: Best and worst-case scenario for GAIA/GAIA-NIR.

$$R_b = \frac{(P_{RX}/N_0)}{(E_b/N_0)}\,, \tag{5.5}$$

and the occupied bandwidth as

$$B = \frac{1.5R_b}{e}\,, \tag{5.6}$$

where, e is the spectral efficiency, whose values can be found in Tab. 4.1, and 1.5 is the AWGN occupied bandwidth with respect to the channel symbol rate for $m_{RG} = 0.444$ as computed in Chapter 4 and reported in Tab. 4.2.

Considering the ESA's mission GAIA, the bitrate achieved by implementing the GMSK modulation is constrained to 8.75 Mbps [4]. The preliminary results in Tab. 5.2 highlight how the proposed system breaks this limit, allowing a doubling of the data rate for the GAIA's best-case scenario. The big advantage, though, can be seen in GAIA-NIR, where the greater EIRP allows higher-order modulation schemes to be used, such as 16-APSK and 32-APSK, for the worst and the best-case scenario respectively. For the latter, it can be seen in Tab. 5.2 that the bitrate is more than tripled with respect to the rate bound currently achieved by GAIA, proving the considerable improvement of the SCCC-PN Ranging scheme.

Moreover, even though GAIA does not incorporate the PN Ranging, the timing jitter performance has been analyzed for both the missions. It is reminded that the received signal (neglecting the noise) is

$$\begin{aligned} x_{TM}(t)r_{RG}(t) &= x_{TM}(t)e^{jm_{RG}\Phi_{RG}(t)} && (5.7)\\ &\approx x_{TM}(t)\left[J_0(m_{RG}) + j2J_1(m_{RG})\Phi_{RG}(t)\right]. && (5.8)\end{aligned}$$

where in the last step, the Jacobi-Anger identity was adopted by considering that the ranging chips use sinusoidal pulses. It can be observed that $r_{RG}(t)$'s most significant component is the imaginary one since the real part is discarded at the receiver. Thus, the received useful power of the ranging signal P is scaled, with respect to the power of the received signal P_{RX}, by a factor $2J_1^2(m_{RG})$. This reads as

$$P/N_0 = P_{RX}/N_0 - 10\cdot\log_{10}(2J_1^2(m_{RG}))\ [\mathrm{dB}]\,. \tag{5.9}$$

The specifications considered for implementing the ranging system in the two missions are reported in Tab. 5.3. For evaluating the tracking performance of the ranging system, the timing jitter has been computed by taking the value obtained from equation (4.26) and normalizing it with respect to the chip time (T_c; $\widetilde{\sigma}_\tau^2$). An additional 1 dB has been subtracted to account for

Parameter	Value
m_{RG}	0.444 rad-pk
R_c	3 Mchip/s
B_L	1.5 kHz

Table 5.3: Ranging system parameters setting for GAIA and GAIA-NIR.

	GAIA		GAIA-NIR	
	Best-case	Worst-case	Best-case	Worst-case
P/N_0B_L [dB]	39.7	33.9	50.8	44.9
Timing Jitter $\widetilde{\sigma}_\tau^2$ [dB]	-46.9	-41.7	-43.9	-43.1
Jitter [m]	0.45	0.83	0.65	0.70

Table 5.4: Ranging jitter performance in GAIA and GAIA-NIR scenarios.

further implementation losses due to the closed-loop receiver of Fig. 4.2. It is worth mentioning that the upper-bound found for the timing variance represents a pessimistic approximation for the P/N_0B_L values considered in Tab. 5.4. In fact, for the range of interest, the simulated timing jitter curve of the modulation formats taken into account already converges to the ideal one. Nevertheless, for lower P/N_0B_L a better accuracy can be obtained if referring to the values extracted from the simulated curves presented in Section 4.3.

Tab. 5.4 presents the ranging accuracy obtained in the best and worst-case scenarios for both, GAIA and GAIA-NIR. It can be observed that the measure in meters of the jitter can be easily obtained by using the following conversion formula:

$$\text{Jitter} = \widetilde{\sigma}_\tau T_c \cdot c \,[\text{m}]\,, \tag{5.10}$$

where $\widetilde{\sigma}_\tau$ is the normalized ranging standard deviation.

For Science missions the ranging accuracy generally must be lower than 5 meters, therefore, it is clear that the ranging performance is not harmed at all by deploying the SCCC-PN Ranging system rather than the standard one. Indeed, the accuracy is always kept under the meter, and the bitrate, as already pointed out, has far exceeded the current rate bound.

Conclusions

In this thesis, it has been studied and analyzed the feasibility of implementing the PN Ranging coupled with high-order modulation schemes (SCCC modulations). For this purpose, a new communication architecture was defined: on the transmitter side, the complex base-band SCCC-modulated telemetry stream has been multiplied by the phase-modulated ranging signal. Instead, at the receiving end, a receiver scheme implementing simultaneous demodulation of high-order telemetry symbols, and tracking of the received ranging sequence for orbit determination, has been designed. The results obtained can be evaluated from the ranging and the telemetry performance point of view. For what concerns the former, the simulations carried out for the SCCC-PN Ranging system showed that it is possible to achieve a ranging accuracy comparable to the classical approach of using the GMSK modulation. In particular, it has been observed how the timing variance decreases by lowering the loop bandwidth B_L because of the averaging effect on the high-order modulation's varying envelope. For the loop bandwidth, a value of 1.5 kHz proved to offer a good ranging accuracy in the P/N_0B_L range of interest for the GAIA and GAIA-NIR missions, without either introducing excessive noise or requiring a large acquisition time. On the telemetry performance side, the proposed system eliminated the data rate constraint previously imposed by the combination of the GMSK modulation, and the 10 MHz bandwidth constraint. However, the investigation carried out in this thesis was mostly limited to the AWGN channel model and not all the challenges arising from the implementation of the proposed communication architecture have been explored. For this reason, further work on the topic should study the closed-loop receiver's performance when introducing the TWTA and, therefore, non-linearity. Additionally, the Doppler and the Doppler rate profiles will be analyzed, along with the acquisition stage here neglected. To conclude, via the proposed study, has been achieved the goal of demonstrating the possibility of combining the PN Ranging with high order modulations. This novel system, if implemented, would bring significant improvements to the next generation of small/medium missions that will be able to transmit at a rate of 20-30 Mbps, with an improvement of the data return over 100%, thus paving the way to a new generation of SR missions with more ambitious scientific objectives.

Disclaimer

The view expressed herein can in no way be taken to reflect the official opinion of the European Space Agency.

Bibliography

[1] K. Andrews, J. Hamkins, S. Shambayati, and V. Vilnrotter, “Telemetry-based ranging,” in *2010 IEEE Aerospace Conference.* IEEE, 2010, pp. 1–16.

[2] Consultative Commettee for Space Data Systems, “Pseudo-noise PN ranging systems,” CCSDS, Tech. Rep. Blue Book 414.1-B-2, 2014.

[3] European Space Agency, “Gaia NIR. Study to Enlarge the Achievements of Gaia with NIR Survey,” ESA, Tech. Rep. CDF Study Report: CDF-175(C), 2017.

[4] ——, “GAIA flight model payload data handling unit delivered and integrated,” Available at https://sci.esa.int/web/gaia/-/51777-09-gaia-flight-model-payload-data-handling-unit-delivered-and-integrated.

[5] Consultative Commettee for Space Data Systems, “SCCC—Summary of definition and performance,” CCSDS, Tech. Rep. Green Book 130.11-G-1, 2019.

[6] P. Fortescue, G. Swinerd, and J. Stark, *Spacecraft systems engineering.* John Wiley & Sons, 2011.

[7] Consultative Commettee for Space Data Systems, “Pseudo-noise PN ranging systems,” CCSDS, Tech. Rep. Green Book 414.0-G-2, 2014.

[8] European Cooperation for Space Standardization, “Space eegineering. radio frequency and modulation,” 2001.

[9] Space Frequency Coordination Group, “Use of the 8450-8500 MHz band for space research, category A,” 1998, REC SFCG 5-1R5.

[10] Consultative Commettee for Space Data Systems, “Flexible advanced coding and modulation scheme for high rate telemetry applications,” CCSDS, Tech. Rep. Blue Book 131.2-B-1, 2012.

[11] European Space Agency, “GAIA overview,” Available at https://www.esa.int/Science_Exploration/Space_Science/Gaia_overview.

[12] G. Maral and M. Bousquet, *Satellite Communication Systems.* John Wiley & Sons Ltd., 2009.

[13] Jet Propulsion Laboratory, California Institute of Technology, “Autonomous software-defined radio receivers for deep space applications,” JPL, Tech. Rep., 2006.

[14] F. M. Gardner, *Phaselock techniques.* John Wiley & Sons, 2005.

[15] Consultative Commettee for Space Data Systems, "Radio frequency and modulation systems - part 1 Earth stations and spacecrafts," CCSDS, Tech. Rep. Blue Book 401.0-B-30, 2020.

[16] K. Murota and K. Hirade, "GMSK modulation for digital mobile radio telephony," *IEEE Transactions on communications*, vol. 29, no. 7, pp. 1044–1050, 1981.

[17] Consultative Commettee for Space Data Systems, "Simultaneous transmission of GMSK telemetry and PN ranging," CCSDS, Tech. Rep. Green Book 413.1-G-1, 2017.

[18] F. Xiong, *Digital Modulation Techniques.* Artech House, 2006.

[19] Consultative Commettee for Space Data Systems, "Bandwidth-efficient modulations," CCSDS, Tech. Rep. Green Book 413.0-G-2, 2009.

[20] P. Laurent, "Exact and approximate construction of digital phase modulations by superposition of amplitude modulated pulses (AMP)," *IEEE transactions on communications*, vol. 34, no. 2, pp. 150–160, 1986.

[21] E. Perrins and M. Rice, "PAM decomposition of M-ary multi-h CPM," *IEEE Transactions on Communications*, vol. 53, no. 12, pp. 2065–2075, 2005.

[22] Consultative Commettee for Space Data Systems, "Bandwidth-efficient modulations - summary of definition,implementation, and performance," CCSDS, Tech. Rep. Green Book 413.0-G-3, 2018.

[23] S. Benedetto and G. Montorsi, "Iterative decoding of serially concatenated convolutional codes," *Electronics letters*, vol. 32, no. 13, pp. 1186–1188, 1996.

[24] P. Massoud Salehi and J. Proakis, *Digital Communications.* McGraw-Hill Education, 2007.

[25] J. L. Junkins and H. Schaub, *Analytical mechanics of space systems.* American Institute of Aeronautics and Astronautics, 2009.

[26] Consultative Commettee for Space Data Systems, "Radio frequency and modulation systems," CCSDS, Tech. Rep. Blue Book 401.0-B-30, 2020.

[27] European Space Operations Centre ESOC, "ESA Tracking Stations (ESTRACK) Facilities Manual," 2008, DOPS-ESTR-OPS-MAN-1001-OPS-ONN.